Chapter 4 - Biological evaluation of the synthesized compounds.

4.1 Determination of ion channel activity.

Different evaluation and characterization techniques of the activity and behavior of ion channels have been developed. From all of them, electrophysiological techniques are the most employed to accurately evaluate ion flux through cell membranes. This technology is unique since it allows single-channel measurements of currents that are in the picoamperes (pA) range.

Voltage clamp, one of these electrophysiological techniques, consists on the isolation of a small portion of cell membrane, containing one or more ion channels, using a glass micropipette as electrode. After isolation of the patch, the current through the membrane is recorded. In general, this method allows ion flow across the cell membrane to be measured as electric current, whilst the membrane voltage is held under experimental control with a feedback amplifier (Figure 84). Since its original design, many variants of the technique have evolved and voltage clamp analysis has been extended to a wide range of tissues.
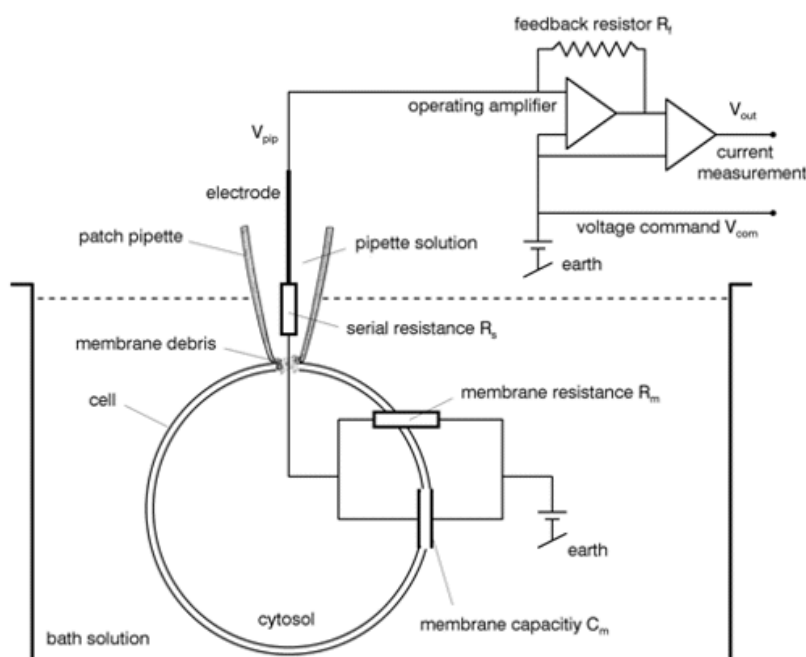

Figure 84. Simplified diagram of a patch-clamp amplifier and a substitute circuit of a whole-cell configuration: R_f: feedback resistor, V_{com}: command voltage, V_{pip}: pipette potential, V_{out}: output voltage proportional to the current. The circuit of the amplifier represents a so-called current-to-voltage converter, which is installed in a little box (preamplifier) near the pipette. After breaking through the membrane, the whole-cell configuration is obtained.

The usefulness of the voltage clamp method stems firstly from the fact that it allows the separation of membrane ionic and capacitive currents. Secondly, it is much easier to obtain information about channel behavior using currents measured from an area of membrane with a uniform, controlled voltage, than when the voltage is changing freely with time and between different regions of the membrane. This is especially interesting because the opening and closing (gating) of most ion channels is affected by the membrane potential.

The isolation of a patch of membrane is achieved by pressing a fire-polished glass pipette, which has been filled with a suitable electrolyte solution, against the surface of a cell and applying light suction. Providing that both a glass pipette and cell membrane are clean, a seal whose electrical resistance is more than 10 gigaohm (GΩ) is formed. This seal is commonly referred as gigaohm seal and is required for the following reasons:

a) The higher the seal, the more complete is the electrical isolation of the membrane patch.

b) A high seal resistance reduces the current noise of the recording, allowing good time resolution of single channel currents.

When the patch is formed, voltage is fixed at a certain value and then the desired stimulus is applied.

4.1.1 TRPV1 voltage clamp.

As stated before, TRPV1 can be activated by diverse stimuli. When some of those stimuli are applied, the channel opens, leading to an entrance of calcium ions to the cytoplasm media. This flux of ions generates a current, allowing the generation of dose response graphs for different stimulus (Figure 85). Among the different activating stimuli, capsaicin is the most used agent to activate the TRPV1 channel. In this thesis, activity recordings were collected by delivering a constant dose of capsaicine and simultaneous administration of a known concentration of the interest product, recording the variations of the measured current.
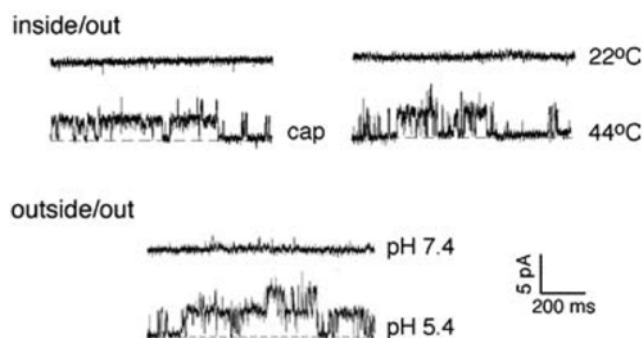
Figure 85. TRPV1 currents evoked by capsaicin (cap, 100 nM), heat (44°C) or acid (pH 5.4) at +40 mV in inside/out (cap and heat) or outside/out (acid) configurations. Broken lines indicate closed channel level. Extracted from Tominaga et al.[141]

Different cells had been employed to express TRPV1, e.g. HEK293,[142] Xenopus Oocytes,[143] Chinese Hamster Oocytes (CHO)[144] or, more recently, the SH-SY5Y cells.[145] Due to availability and the large size of the cells (1.0 mm diameter), Xenopus Oocytes were the cells chosen to express human TRPV1 in this project. All the cloning, expression and electrophysiological assays on TRPV1 were carried out in collaboration with the group of Professor Ferrer-Montiel, from the Universidad Miguel Hernandez (Elche), using procedures developed by the same group.[146]

4.2 Activity evaluation of trisubstituted triazines.

The inhibitory activity of each triazine was evaluated by voltage-clamp against rat TRPV1 channels heterologously expressed in *Xenopus* oocytes. Once the transfected cell was clamped, a dose of capsaicin was given in order to trigger the opening of the channel that led to the corresponding evoked current. As illustrated on Figure 85, instillation of capsaicin onto oocytes expressing TRPV1 channels generated a large inward current that was rapidly blocked in a dose dependent-manner by application of triazine compounds. Thus, triazines **40**, **46** or **61**, for example, seemed to be able to compensate the effect of capsaicin in a dose dependent manner. However, it was noticeable (Figure 86) that **46** was able to block capsaicin evoked currents in a more efficient way than **40** or **61**. At doses of 0.1 μM, **46** was able to reduce the currents to less than half of the initial value while at the same dose neither **40** nor **61** were able to achieve the same results. Indeed, as it will be shown later in more detail, the blocking activity of **46** resulted to be ten fold higher than that of **40** or **61**.
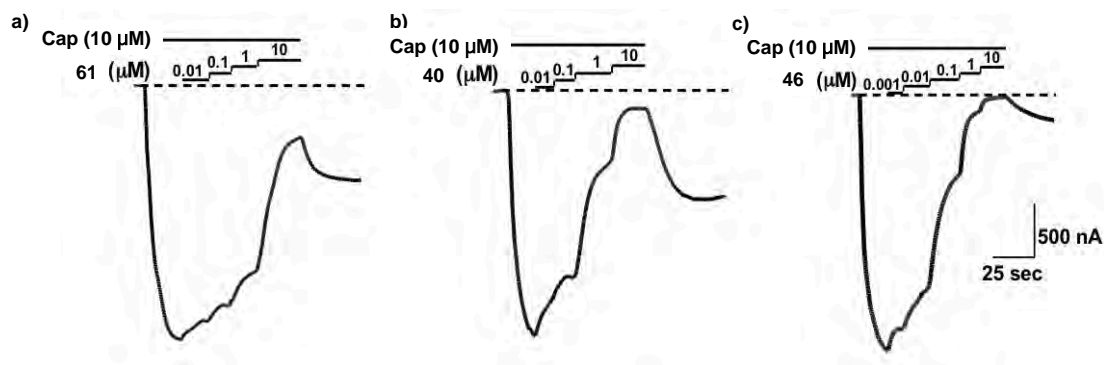
Figure 86. Representative ionic currents and blocking of capsaicin-evoked responses by compounds **61** (a), **40** (b), and **46** (c) at concentrations between 0.01-10 µM. Ionic currents were elicited in oocytes heterologously expressing TRPV1. The holding potential was -60 mV. The concentration of capsaicin was 10 µM. The horizontal bars indicate the experimental paradigm used for agonist stimulation and channel blocking.
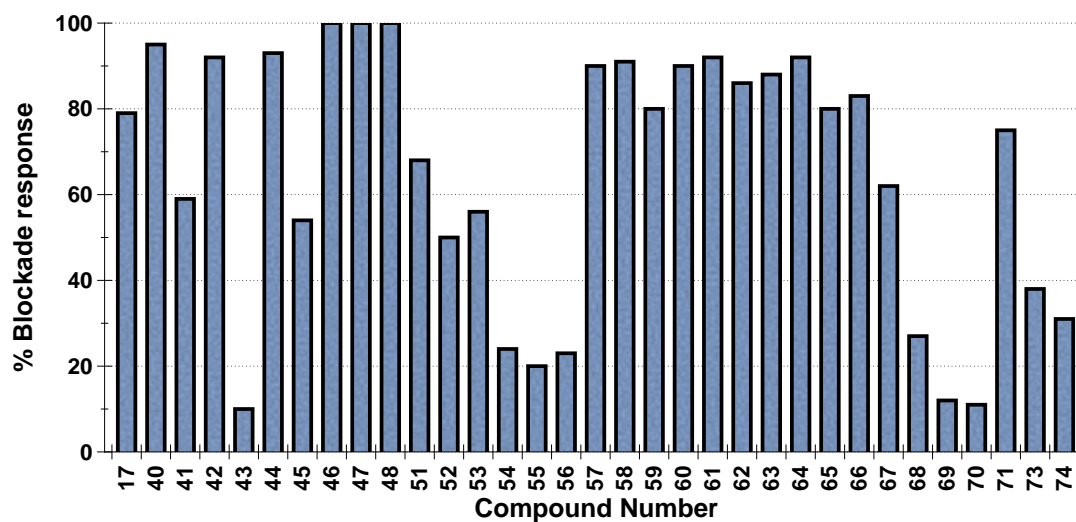

Figure 87. Blockade of capsaicin evoked currents on TRPV1 by the synthesized triazines. Conditions: [cap] = 10 µM, [triazine] = 10 µM.

	R₁-X = R₁'-X		R₂-X		R₁-X = R₁'-X		R₂-X

The structures are shown with the core 1,3,5-trisubstituted benzene bearing R_1-X, R_1'-X and R_2-X substituents.

No.	R	n	R_2-X	No.	R	n	R_2-X
17	2,4-Cl₂	2	Me₂N-(CH₂)₃-NH-	58	2-F	2	Me₂N-(CH₂)₃-NH-
40	4-Cl	2	Me₂N-(CH₂)₃-NH-	59	4-NO₂	2	Me₂N-(CH₂)₃-NH-
41	4-Cl	2	Me₂N-(CH₂)₂-NH-	60	4-MeO	2	Me₂N-(CH₂)₃-NH-
42	4-Cl	2	(N-methylpyrrolidinyl)ethyl-NH-	61	H	2	Me₂N-(CH₂)₃-NH-
43	4-Cl	2	piperazinyl	62	4-Cl	1	Me₂N-(CH₂)₃-NH-
44	4-Cl	2	H₂N-ethyl-piperazinyl	63	4-F	1	Me₂N-(CH₂)₃-NH-
45	4-Cl	2	amino-piperazinyl	64	2,4-Cl₂	1	Me₂N-(CH₂)₃-NH-
46	4-F	2	Me₂N-(CH₂)₃-NH-	65	2,4-F₂	1	Me₂N-(CH₂)₃-NH-
47	4-Cl	2	Me₂N-(CH₂)₅-NH-	66	4-F₃C	1	Me₂N-(CH₂)₃-NH-
48	4-F	2	guanidino-propyl-NH-	67	(benzodioxolylmethyl)-NH-		Me₂N-(CH₂)₃-NH-

No.	R	n	R_2-X
68	R = Me		Me₂N-(CH₂)₃-NH-
69	R = H		Me₂N-(CH₂)₃-NH-
70	R = H		Me-(CH₂)₃-NH-

No.	R	n	R_2-X
50	4-F	2	Me₂N-(CH₂)₃-O-
51	4-F	2	Me₂N-(CH₂)₂-O-(CH₂)₂-NH-
52	4-F	2	Me₂N-ethyl-piperazinyl
53	4-F	2	piperidinyl-piperazinyl
54	4-F	2	HO-(CH₂)₃-NH-
55	4-F	2	CH₃-(CH₂)₂-NH-
56	4-F	2	CH₃-(CH₂)₅-NH-
57	3-F	2	Me₂N-(CH₂)₃-NH-

No.	R_1-X = R_1'-X	R_2-X
71	(indol-3-yl)ethyl-NH-	Me₂N-(CH₂)₃-NH-
72	tetrahydro-β-carbolinyl	Me₂N-(CH₂)₃-NH-
73	bis(4-fluorophenyl)methyl-piperazinyl	Me₂N-(CH₂)₃-NH-
74	(cyclohexenyl)ethyl-N-	Me₂N-(CH₂)₃-NH-

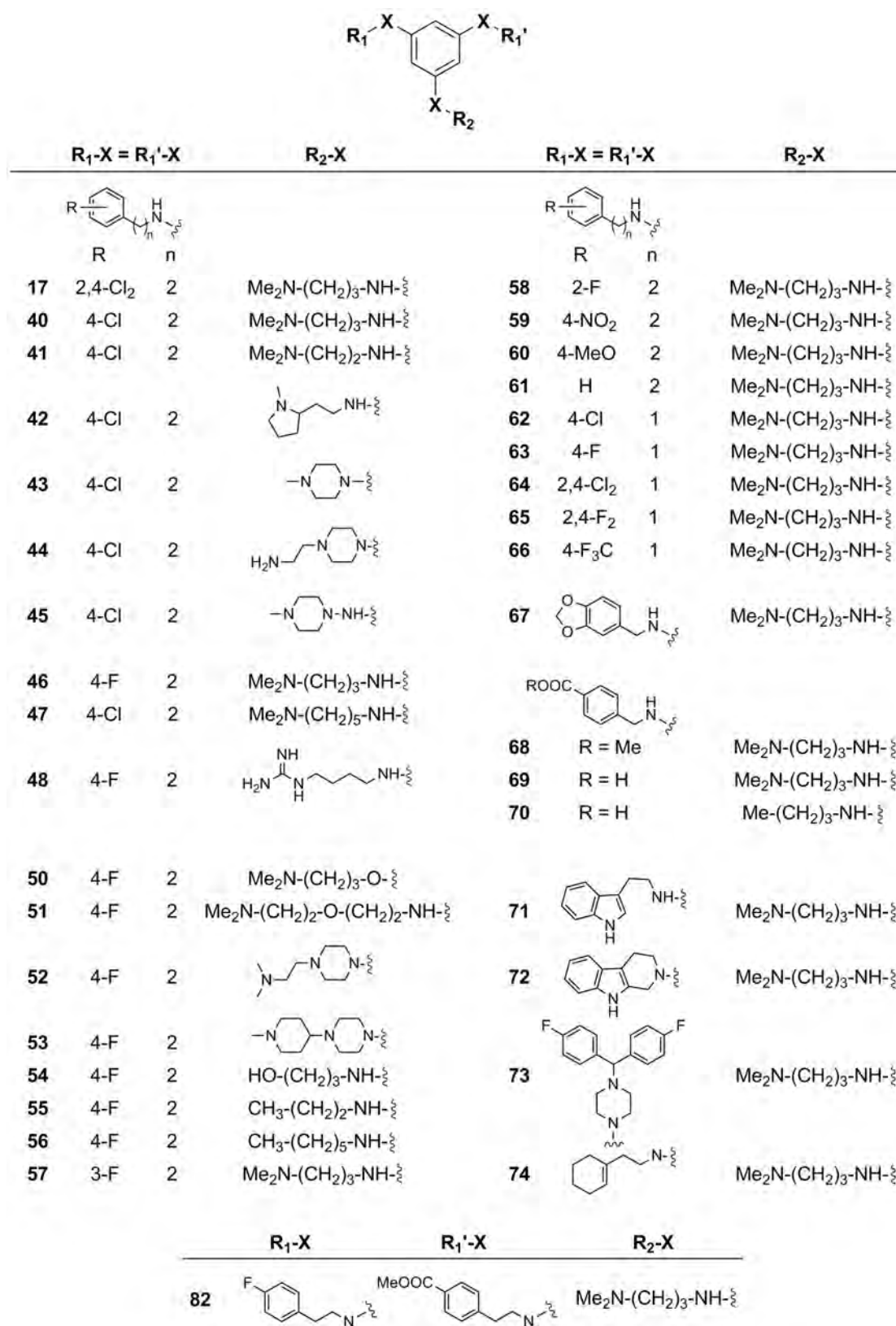|	R_1-X	R_1'-X	R_2-X
82	(4-F-phenyl)ethyl-N	(MeOOC-phenyl)ethyl-N	Me₂N-(CH₂)₃-NH-

Figure 88: Structures of the 1,3,5-trisubstituted triazines evaluated as antagonist of TRPV1.

105

Screening of the components of the library of trisubstituted triazines (Figure 88) to find blockers of the TRPV1 capsaicin evoked currents was initially performed at a single concentration of 10 µM. As shown in Figure 87, 14 products blocked more than 80 % of the capsaicin evoked current, and only 9 products exhibited a blocking activity under 40 %. Among the most active compounds, aside from **46**, two additional triazines, **47** and **48**, exhibited 100 % of channel blockade. Structurally the three triazines were very similar, being the main difference the length of the alkyl chain that connects the protonable dimethylamino group to the triazine ring or the replacement of this group by a guanidino group. On the other hand, 3 triazines (**43**, **69** and **70**) also showed a blocking capacity only around 10 %. Two of them (**69** and **70**) shared in common the presence of a carboxylic acid group bound to both aromatic rings, while the third (**43**) had a more rigid piperazine ring replacing the dimethylaminopropyl moiety present in the most active analogs. The activities and structures of the rest of compounds were more variable and their SAR relations are discussed in more detail below. Finally, it is worth mentioning that the results of this screening were generated in parallel to the sinthesis of compounds, and were used as initial criteria of their potency, helping to guide the design of new triazines.

Previously described TRPV1 antagonists **DD161515**, **DD191515** and **H-Arg-15-15** had shown a promising activity blocking the capsaicin evoked current (Figure 89a), but when applied at low concentrations, where the antagonist effects were lower, they exhibited an agonistic effect, slightly activating the channel (Figure 89b). This effect has pro-inflammatory characteristics and is undesired as it is related to the itching and burning sensation of capsaicin treatment. In order to know if the newly synthesized compounds did exhibit this behavior, they were tested in the absence of capsaicin to evaluate their TRPV1 activation capacity (Figure 91).
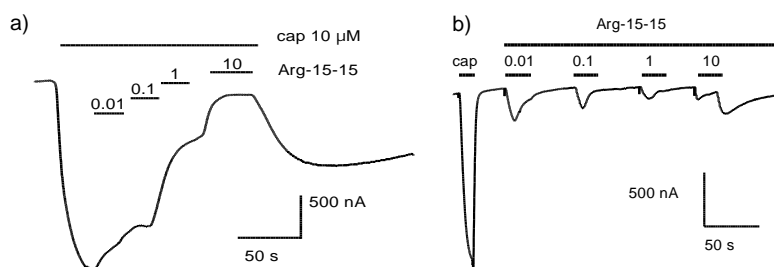

Figure 89. a) Blockade of capsaicine evoked current by peptoid H-Arg-15-15 at concentrations between 0.01-10 µM. b) Activation of TRPV1 at low concentration of antagonist H-Arg-15-15; a capsaicin pulse (10 µM) was applied as reference to compare the TRPV1 activating effect of the compound.

Figure 90 shows the results from three voltage clamp TRPV1 activation experiments for triazines **40**, **46** and **61**. While triazine **61** showed a significant agonist activity, **40** and, particularly, **46** showed a lower or almost null TRPV1 activation effect. Remarkably, triazine **46** was one of the few, amongst all the triazines assayed, with almost no TRPV1 activation effect at low doses, becoming a "pure" blocker of TRPV1.
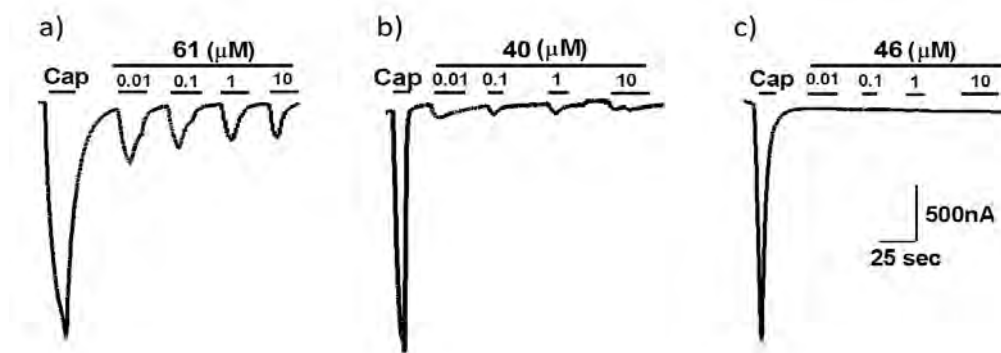

Figure 90. Voltage-clamp experiments performed with different doses (0.01-10 µM) of **61** (a), **40** (b) and **46** (c) in the absence of capsaicin to determine their agonistic effects on TRPV1. The response to a capsaicin pulse (10 µM) is also shown for comparison.
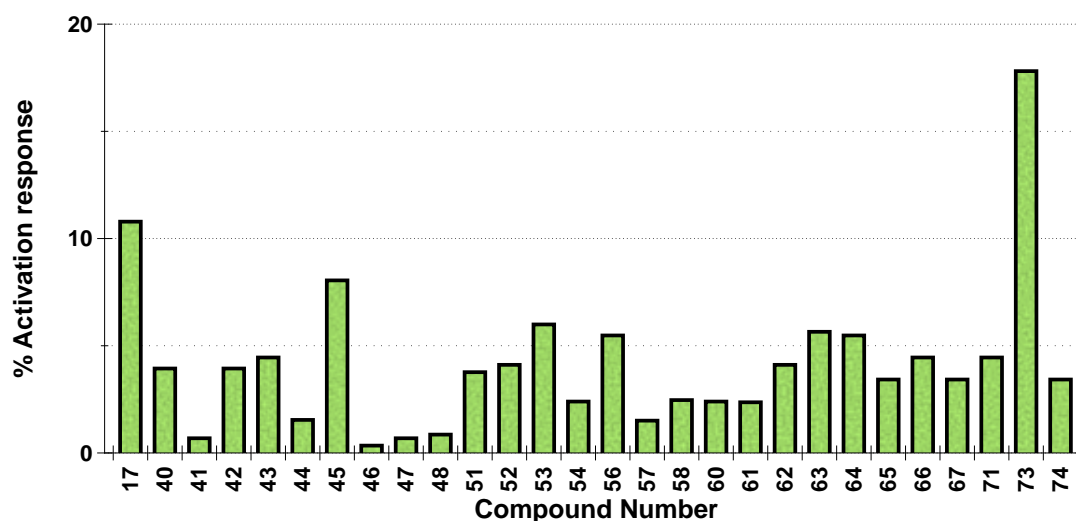
Figure 91. TRPV1 agonistic activity shown by the synthesized triazines at 10 µM.

At 10 µM, most triazines exhibited low TRPV1 activation, i.e. below 5% (Figure 91), and 4 of them showed activitations below 1%, namely triazines **41**, **46**, **47** and **48**. As mentioned above, triazines **46**, **47** and **48** were also those which showed 100 % blocking activity at 10 µM, therefore these three compounds became very promising hits as TRPV1 antagonist. On the other extreme, the bulkiest triazine **73** exhibited the largest activation, generating currents near 20% of the capsaicin evoked current at the

same dose, and triazine **15**, with a structure closer to that of active compounds such as **46**, was the second one showing an agonist activity around 11 %.

To further asses the TRPV1 blocking capacity of the synthesized triazines, their dose response curves were determined (see Annex 3), and the half maximal inhibitory concentrations (IC_{50}) were evaluated as a measure of their potency as TRPV1 antagonists. All compounds were evaluated at least at 5 different concentrations and 6 replicates were performed at each concentration. The upper concentration limit of these assays was around 200 µM, due to solubility. This made difficult to determine the IC_{50} values for the less active compounds, therefore, the uncertainty of those is in some cases quite high. As example, dose-response curves for products **40**, **46** and **52** are represented in Figure 92. These curves evidence the different potencies as antagonist of the TRPV1 currents evoked by capsaicin that these triazines exhibit, spanning more than two orders of magnitude inspite of their closely related structures (cf. **46** vs **40**).
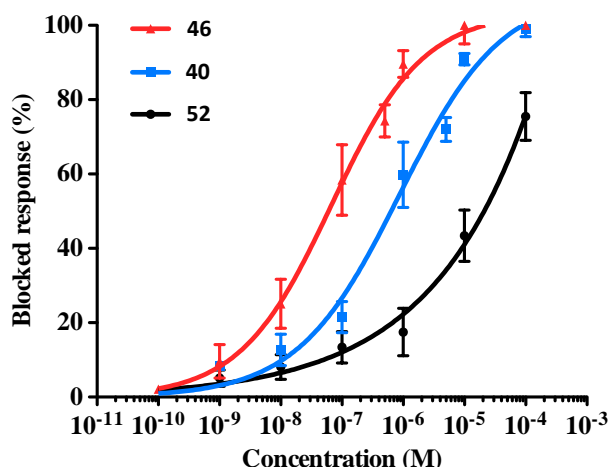

Figure 92. Dose response curves for products **46**, **40** and **52** as antagonist of the TRPV1 current evoked by 10 µM capsaicin.

Table 10 collects the IC_{50} values determined for each triazine, as well as their antagonist and agonist activities at a fixed concentration of 10 µM. In this table, compound **46** is confirmed as the most active of all the series, with an IC_{50} value of 50 nM. Considering that, as it will be shown below, the TRPV1 blockade elicited by triazine **46** occurs through an uncompetitive mechanism, its potency was among the best reported so far for uncompetitive TRPV1 blockers.[147-149] Furthermore, in Table 10 there are also 10 additional potent triazines (**40**, **44**, **47**, **48**, **57**, **58**, **60**, **61**, **64** and **66**), with IC_{50} values below 1 µM, while the rest show values that span several orders of

magnitude, even above the mM range, indicating that the SAR information contained in this set could be highly informative for further development of new TRPV1 antagonists.

Table 10. Summary of biological data of trisubstituted triazines determined by the voltage clamp methodology. Activation and blockade were measured at a fixed dose of 10 µM.

Product	% Blockade	% Activation	IC_{50} µM	Product	% Blockade	% Activation	IC_{50}
17	79	10.8	1.2 ± 0.2	58	91	2.5	0.45 ± 0.07
40	95	3.9	0.5 ± 0.2	59	80	---	1.63 ± 0.37
41	59	0.7	6.7 ± 2.4	60	90	2.4	0.97 ± 0.19
42	92	3.9	1.2 ± 0.03	61	92	2.4	0.67 ± 0.06
43	10	4.5	$1.4 \cdot 10^7 \pm 5.8 \cdot 10^4$	62	86	4.1	2.62 ± 0.94
44	93	1.5	0.96 ± 0.21	63	88	5.7	3.06 ± 0.22
45	54	8.0	6.4 ± 2.4	64	92	5.5	0.84 ± 0.18
46	100	0.3	0.05 ± 0.007	65	80	3.4	3.3 ± 0.61
47	100	0.7	0.1 ± 0.04	66	83	4.5	0.66 ± 0.11
48	100	0.9	0.6 ± 0.06	67	62	3.4	4.98 ± 0.67
50	---	---	6.14 ± 0.7	68	27	---	59.1 ± 29.6
51	68	3.8	7.0 ± 2.99	69	12	---	178 ± 47
52	50	4.1	18.6 ± 6	70	11	---	229 ± 23
53	56	6.0	70.9 ± 9.1	71	75	4.5	2.33 ± 1.23
54	24	2.4	1488 ± 774	72	---	---	7 ± 2.9
55	20	---	2173 ± 1745	73	38	17.8	56.4 ± 14
56	23	5.5	5761 ± 6716	74	31	3.4	218 ± 104
57	90	1.5	0.3 ± 0.04	82	---	---	1.45 ± 0.71

4.3 SAR analysis of the library of TRPV1-antagonist.

Analysis of the triazine anti-TRPV1 potency results contained in Table 10 allowed extracting qualitative SAR information. First, in agreement with the postulated pharmacophore, it was apparent that replacement of the tertiary amine by a polar non-ionizable group or an apolar alkyl moiety, either on the peptoid (cf. **12** vs **14** or **15**, Figure 29, pp. 47) or the triazine series (cf. **46** vs **54**, **55** or **56**), results in an important decrease, or complete loss, of activity (i.e. up to 40000-fold). The high pK_a of the protonable tertiary amino group present in most of the active triazines ensures that this group will be ionized (see triazine calculated pK_a values on Annex 3). Therefore, these results evidence the requirement of a cationic group to achieve high anti-TRPV1 potencies.

On the contrary, changes on the length of the alkyl chain that supports the tertiary amine had a relatively minor effect (cf. **46** vs **47**, or **40** vs **41**). Similarly, changes on the tertiary amine group (cf. **40** vs **42**) or its replacement by a guanidyl

group (cf. **47** vs **48**) afforded a relatively small decrease of activity. The replacement of nitrogen by oxygen as the atom that links the dimethylaminopropyl moiety to the triazine (cf. **46** vs **50**) resulted in a substantial decrease of activity (~120-fold), suggesting a significant role of this nitrogen atom on binding. A similar decrease of activity (~70-fold) was observed by introducing an oxygen atom in the chain that supports the trimethylamino group (cf. **47** vs **51**). Conformational restriction of the flexibility of the alkyl chain that contains the ionizable group, by introducing a cycloalkyl linker, also rendered a decrease in activity (cf. **47** vs **52** or **40** vs **44**), which was greater or much greater for the more restricted analogs (i.e. **53** and **43**), suggesting steric interactions with the channel that could be determinant for the activity.

With respect to the arylalkyl moieties, the >300-fold decrease on activity of compound **74** relative to **61** evidenced the importance of the aromatic groups. The substitution on the aromatic moiety as well as the length of the alkyl linker seemed less important since compounds **17**, **40**, **57**, **58**, **59, 60**, **61**, **62**, **63**, **64**, **65** and **66** showed activities that are within one order of magnitude. In this sense, compounds carrying a carboxylic acid (**69**, **70**) or a carboxylic ester (**68**) are an exception since they showed a ≥100-fold decrease in activity relative to their unsubstituted counterpart (**61**). Larger bicyclic aromatic systems (**67** or **71**), rigid fused tricyclic systems (**72**) or even the bulkiest and quite rigid bis-aromatic substituted triazine (**73**) did not show such a large loss of activity, which suggests that these moieties might occupy sites on the TRPV1 receptor that are relatively open and sterically unrestricted. In any case, it was difficult to define the role of the aromatic substituents and of the triazine ring in binding by this type of analysis. This could be expected since most of the compounds considered contain the triazine core and two aromatic rings which, as previously said, show little influence in activity when their substituents are modified. However, the low activity elicited by compound **74**, the only one without aromatic substituents, suggested that these aromatic groups must play a role in binding.

To get further knowledge on the triazine structural determinants of their anti-TRPV1 activity, a 3D-QSAR study was carried out which is described in the next chapter.

4.4 Further studies on the biological activity of triazine 46.

Triazine **46** was the most potent TRPV1 blocker synthesized with almost no agonist effects at low doses. This generated great expectation and led to further investigations on the interaction between **46** and TRPV1. Which is the blocking ability of **46** against other physiological agonists than capsaicin? How selective is **46** against other Ca^{2+} channels relevant and similar to TRPV1? How does **46** bind to TRPV1 and by which mechanism interacts?

4.4.1 Blockade of pH evoked current by triazine 46.

To answer the first question, triazine **46** was tested against pH mediated TRPV1 activation. Acidic pH predominates at inflammatory loci and other sites of immune activity.[150] If **46** can block both capsaicin (agonist) and pH evocated currents, it would exhibit a polymodal mode of action that can lead to a better desensitization of the affected zone under inflammation conditions.

To evaluate this blocking ability a patch clamp experiment was performed using TRPV1-transfected *Xenopus oocytes* at pH 5.40. Figure 93 shows the dose response curve from this evaluation, probing that **46** can block the TRPV1 pH-evoked current in a dose dependent manner. However, although its potency is still in the micromolar range (IC_{50} (pH) = 0.9 ± 0.2 µM), it is around 20 times less effective than blocking the capsaicin evoked currents.
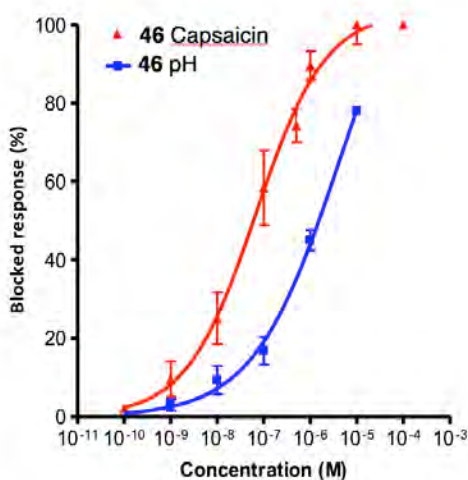

Figure 93. Dose-response curves of triazine **46** as antagonist of the TRPV1 currents evoked by capsaicin (red) and pH 5.40 (blue).

4.4.2 Blockade of mechanical evoked current by triazine 46.

Polymodal nerve fibers are neurons activated by different types of stimuli such as heat, mechanical pressure, or chemical mediators of inflammation, as a result of tissue injury. The ability of those cells to sense multiple external stimuli is related to the expression of many ion channels on its surface that can transduce the different signals.[151] In comparison with patch clamp experiments on TRPV1 transfected cells, polymodal nerve fibers behave as a more complex system for in vivo testing where TRPV1 is expressed among other channels. Although it is well accepted that under normal conditions TRPV1 does not take part on mechanical stimuli sensing,[152] recent studies point in the direction that it can be implied on mechanical stimuli sensing under repeated stimulation.[153]

Currents obtained from the mechanical stimulation of rat knee joint nociceptor fibers were used to evaluate if triazine **46** can block mechanical induced pain signal. Recordings on the rat knee joint with instillation of 10 µM capsaicin provoked an increase in nerve activity that was gradually attenuated up to 50% of the initial activity upon repeated applications of the vanilloid, reflecting the well known process of capsaicin-induced tachyphylaxia[24]. In the presence of 10 µM of **46**, the decrease of capsaicin evoked nerve activity was significantly higher (up to 75%) than that induced by the receptor tachyphylaxia, indicating an inhibitory activity of the triazine **46** *in vivo* (Figure 94a).

After the initial recordings the mechanical stimuli was applied. This consisted in a normal and noxious outward and inward rotation of the knee joint lasting 10 s. As the mechanical assay is performed once, triazine **46** should not be able to interfere in induced mechanical stimulation.[152] In contrast, the triazine did not affect the impulse discharge evoked by mechanical stimulation (Figure 94b), indicating a differential blockade response of triazine **46** in front of different type of stimuli. Despite its inability to antagonize some type of stimuli (i.e. mechanical), being able to block both agonist (i.e. capsaicin) and pH evoked currents, **46** could be classified as a polymodal TRPV1 blocker.
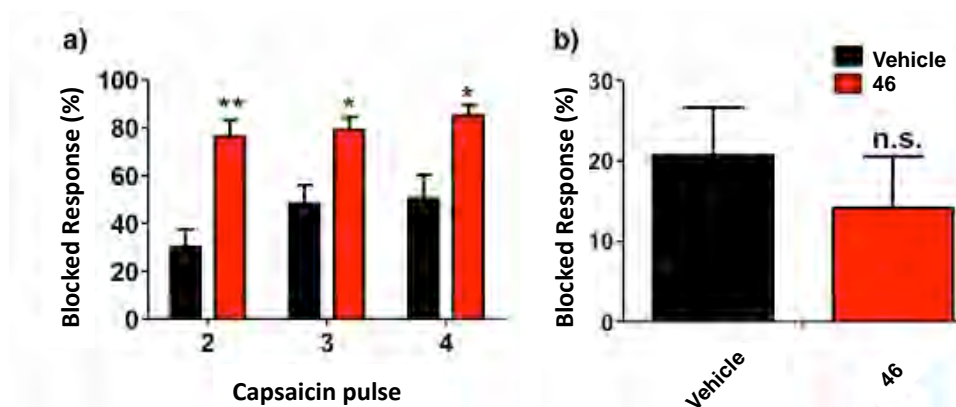
Figure 94. Inhibition by triazine **46** of capsaicin-evoked neural activity in knee joint nociceptor fibres. Quantitative assessment of **46** blockade of capsaicin and mechanically-evoked responses from nociceptor fibres. Data are given as mean±sem, with n (number of animals) ≥5. * P <0.05, ** P ≤ 0.01, 2-Way ANOVA, followed by the Bonferroni post test; n.s. means no significant.

4.4.3 Mechanism of anti-TRPV1 activity of triazine 46.

To determine if **46** is an open-channel blocker, the blocking dependency against voltage was investigated. Open-channel blockers sense the membrane electric field, exerting their activity within a defined range of voltages. The blocking efficacy of positively charged channel blockers is clearly stronger at negative membrane potentials than at positive ones (V ≥ 0 mV). A commonly used model to describe voltage-dependent blockade is the Woodhull model.[154] In this model it is assumed that the charged blocking particle enters the channel pore to a certain distance, and senses part of the transmembrane electric field. According to the Woodhull model, the IC_{50} of a molecule with valence **z**, binding to a site within the membrane electric field is described by the relations stated in Equation (iv) and Equation (v).

Equation (*iv*) $$IC_{50}(V_m) = IC_{50}(0\ mV) \times \exp\left(\frac{z\delta V_m F}{RT}\right)$$

Equation (*v*) $$\frac{I(c)}{I(0)} = \frac{1}{1 + \frac{c}{K_D(0)}} \exp\left(\frac{z\delta V_m F}{RT}\right)$$

Equations *iv* and *v*: Woodhull model used to estimate the electrical distance (δ) of the drug binding site from the entrance to the channel and the dissociation constant at zero voltage ($K_D(0)$).

$IC_{50}(V_m)$ and $IC_{50}(0\ mV)$ are the half-maximal blockade at transmembrane voltage Vm and at 0 mV. δ is expressed as "part per unit" of the way across the membrane's potential from extracellular side to the citoplasmatic side. It represents the location of the energy barrier for block (i.e. the blocker binding site) expressed as a

113

fraction of the electrostatic field gradient sensed by the blocking site. *I(c)* and *I(0)* are the currents with the channel blocker at a concentration *c* or without blocker, respectively. K_D*(0)* is the dissociation constant at zero voltage. *RT/F* is a constant of value 25.3 mV at 20°C.

As depicted in Figure 95a, **46** blocks TRPV1 at negative membrane potentials, yet it is nearly inactive at depolarized (positive) membrane voltages, indicating that its activity is strongly voltage-dependent. Indeed, plotting the blocking ratio against the voltage provides a curve that could be approximated by a Woodhull model that yields an electric distance δ = 0.36 for the binding site of **46** within the membrane electric field (Figure 95b). This value is consistent with the interaction site being located relatively deep within the aqueous pore of the channel and with an uncompetitive mechanism of channel blocking. That **46** acts as an open-channel blocker was further corroborated by the finding that the EC_{50} of capsaicin was not altered by the presence of **46**, indicating that this compound is not a competitive antagonist of capsaicin.
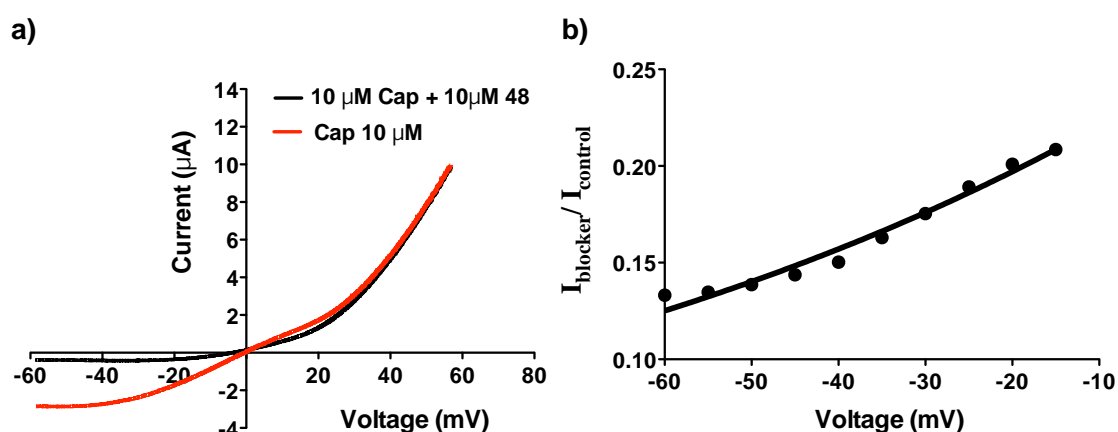

Figure 95. a) Blocking dependence versus membrane voltage of **46**. b) Fitting of a Woodhull model to the obtained data from current vs voltage experiment. The solid line represents the fitting to equation (*v*).

4.4.4 Blocking selectivity against diverse ion channels.

4.4.4.1 Selectivity against TRPM8 and NMDA channels.

To evaluate the selectivity of **46**, it was tested against the TRPM8 and the N-Methyl-D-aspartate (NMDA) receptor channels. Both of these channels are Ca^{2+} selective with some structural resemblance to TRPV1.

TRPM8 is an ion channel that, upon activation, allows the entry of Na^+ and Ca^{2+} ions to the cell, leading to depolarization and the generation of an action potential. This

eventually leads to the feeling of cold. The TRPM8 protein is expressed in sensory neurons, and it is activated by cold temperatures and cooling agents, such as menthol and icilin. TRPM8 knockout mice not only indicated that TRPM8 is required for cold sensation but also revealed that it mediates both cold and mechanical allodynia in rodent models of neuropathic pain. Furthermore, recently it was shown that TRPM8 antagonists are effective in reversing established pain in neuropathic and visceral pain models.[155,156]

The NMDA receptor is a non-specific cation channel, which allows the passage of Ca^{2+} and Na^+ into the cell, and K^+ out of the cell. The excitatory postsynaptic potential produced by activation of the NMDA receptor increases the concentration of Ca^{2+} in the cell. Ca^{2+} can in turn function as a second messenger in various signalling pathways. Calcium flux through the NMDA channel is thought to be critical in synaptic plasticity, a cellular mechanism for learning and memory.[157,158]

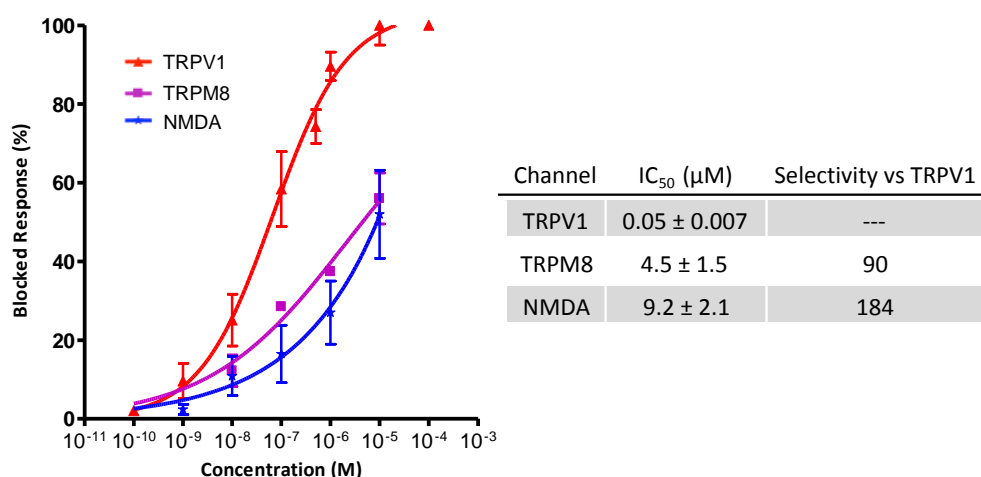| Channel	IC$_{50}$ (µM)	Selectivity vs TRPV1
TRPV1	0.05 ± 0.007	---
TRPM8	4.5 ± 1.5	90
NMDA	9.2 ± 2.1	184

Figure 96. a) Dose-response curves for the blocking of TRPV1 (red), TRPM8 (purple) and NMDA (blue) elicited by **46** at concentrations between 1 nM – 100 µM. b) Values of IC$_{50}$ and selectivity ratio against TRPV1.

Evaluation of **46** on TRPM8 and NMDA activated channels was performed (Figure 96). The comparison of the determined IC$_{50}$ values with that of TRPV1, and a selectivity value calculated as the ratio between the IC$_{50}$ relative to TRPV1 are shown on the right side of Figure 96. As can be observed, triazine **46** was >90 fold more selective for TRPV1 than for the other two channels.

4.4.4.2 Selectivity of triazine derivatives against the hERG channel.

Ion channel Kv11.1 is the alpha subunit of a potassium ion channel commonly known by the name of the gene that codes for it, the human Ether-à-go-go-Related Gene commonly named hERG. This ion channel is best known for its contribution to the electrical activity of the heart that coordinates the heart's beating. hERG K^+ channels are responsible for a rapid component (I_{Kr}) of the repolarizing currents that terminate the cardiac action potential.[159] Drugs that inhibit hERG have the potential to extent the cardiac action potential and the QT interval (Figure 97) and cause "torsade de pointes", a specific type of abnormal heart rhythm that can potentially lead to sudden cardiac death.

Although, for natural occurring torsades de pointes most episodes revert spontaneously to sinus rhythm, in case of pharmacological hERG blocking possible outcomes include palpitations, dizziness, lightheadedness, syncope and sudden death.[160] There exist other potential targets for cardiac adverse effects, but the vast majority of drugs associated with acquired QT prolongation are known to interact with the hERG potassium channel.[161] The reason behind hERG promiscuity is on account of a large cavity in the inner region of the pore. This region is larger than other K^+ ion channels and so it can interact with a wide size-range of drugs.

Because its important role in heart repolarization, since 2005 different measures were taken in order to prevent that new marketed drugs exhibit hERG affinity. Both FDA and the International Conference on Harmonisation (ICH) of Technical Requirements for Registration of Pharmaceuticals for Human Use have stated different protocols to characterize the action of drugs over hERG and restrain their use if considered harmful.[1]
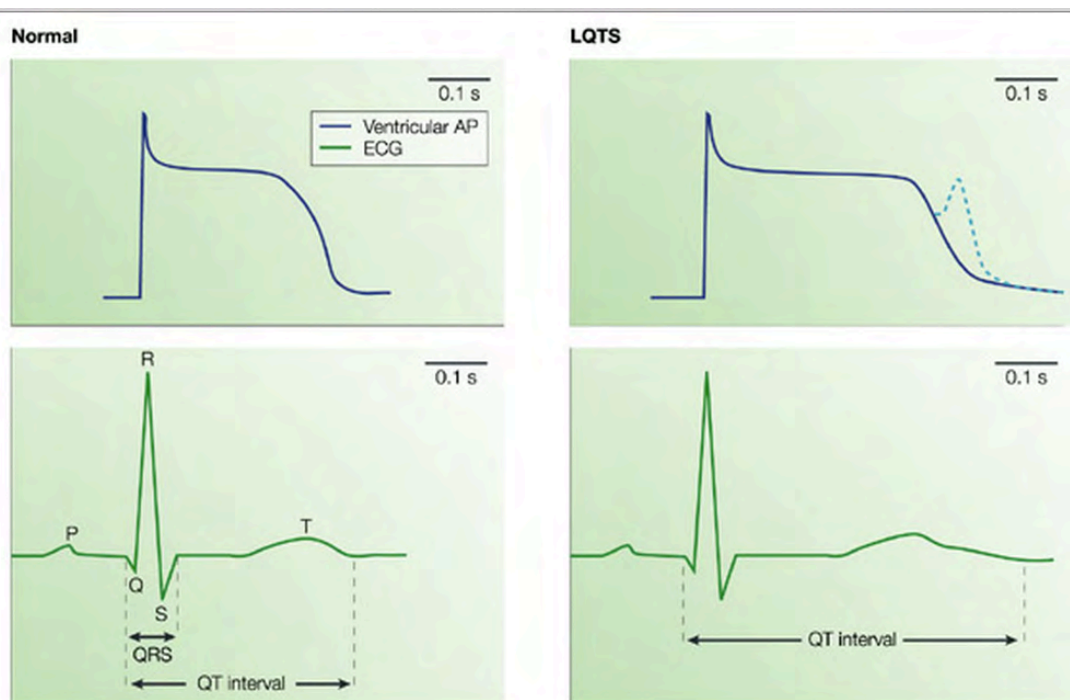
---

[1] ICH ref ucm074963

Figure 97. Ventricular action potential (AP; top panel) and electrocardiogram (ECG; bottom panel) recorded from a normal patient and a patient with long-QT syndrome (LQTS). The QT interval is measured from the start of the QRS complex to the end of the T wave. The QT interval is normally < 0.44 s. In LQTS, abnormalities in currents during the plateau phase lead to prolongation of the ventricular AP and hence the QT interval, as well as increasing the tendency for early after-depolarizations (dotted line), which markedly increases the risk of arrhythmias.[162]

As triazine derivatives are ion channel blockers, it was interesting to know the inhibition profile/selectivity against hERG, as a high blockade activity would represent the restriction of their systemic use for pain management. The *in-vitro* assay used started from oocyte cells stably transfected with the hERG gene. Then by using patch-clamp in whole-cell configuration, the rapid delayed rectifying potassium (I_{Kr}) current inhibition was measured. The cell was clamped at a holding potential of -80 mV and depolarized to voltages between -60 and +60 mV for 1 s to activate hERG current. The cell was then clamped to -50 mV for 2 s to record a tail current. If the channel works correctly, large tail currents are recorded as channel opens, coherently generating a negative exponential current flow. On the contrary, when the experiment is ran in the presence of a hERG channel antagonist what is observed is a rapid response of membrane potential without the corresponding tail current. To compare the blocking activity of triazine compounds, a known hERG blocker (E-4031) was used. Triazines **40**, **46** and **47** blocked the tail currents at 5 µM dose.
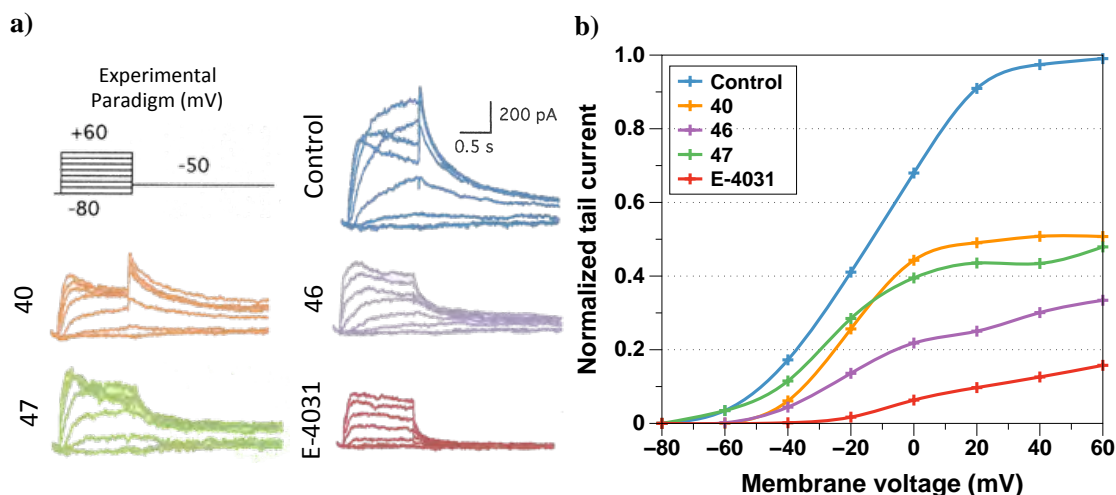
117

Figure 98. hERG currents recorded on hERG transfected oocytes while applying the paradigm depicted on top left area of the figure. b) Compilation of normalized tail currents from the experiments carried out.

From all the previously shown information it can be concluded that **46** is a pseudo selective ion channel blocker with some affinity for the hERG channel. Although a more in depth study of the interaction of **46** with hERG is required to discard **46** for systemic use, the data on hERG activity forced to refocus the applicability of this triazine.

4.4.5 *In vitro* toxicity profile of triazine 46.

Test compounds may have undesired side effects in addition to the desired modulation of TRPV1 signalling pathway. Those undesired side effects could compromise the viability and integrity of some cell/tissues and, in the last extent, the whole organism. Therefore, to characterize the toxicity profile of a new drug candidate is a major issue. Different approaches have been designed to evaluate cell viability and growth and among those the MTT assay is one of most used procedures. This colorimetric microplate assay is cost effective because of the number of tests which can be performed at one time without problems of radio-isotope and contaminated materials disposal. MTT assays measure the reducing potential of the cell using a colorimetric reaction in which NAD(P)H-dependent oxidoreductase enzymes reflect the number of viable cells present. MTT (3-(4,5-dimethylthiazol-2-yl)-2,5-diphenyltetrazolium) is the key compound of this analysis: when it is reduced, it generates a formazan containing product with a characteristic visible absorption band between 500 and 600 nm (Figure 99). This reduction takes place only when mitochondrial reductase enzymes are active. Formazan derivative is insoluble in

cellular media and has to be dissolved previously to determine its concentration. Although MTT method does have limitations influenced by the physiological state of the cells and the variance in mitochondrial dehydrogenase activity, it has proven to be useful in the measurement of cell growth in response to mitogens, antigenic stimuli, growth factors and other cell growth promoting reagents, cytotoxicity studies, and in the derivation of cell growth curves.
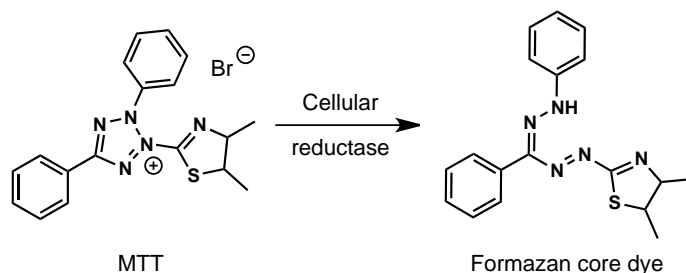

Figure 99. MTT molecule and the corresponding formazan reduced core.

HEK293 cells in 96-well plates were incubated with increasing concentrations of triazine compounds for 24 h to evaluate triazine toxicity. Triazines selected for evaluation with the MTT assay were those exhibiting the higher potencies (i.e. $IC_{50} < 1$ µM, Figure 100). At low dosage, most of them resulted moderately toxic, being its toxicity under 30% until 10 µM. Only triazine **48,** containing the guanidine moiety, is toxic at low doses. This was an encouraging result, as products with small IC_{50} like **46** could be used for further biological evaluation.
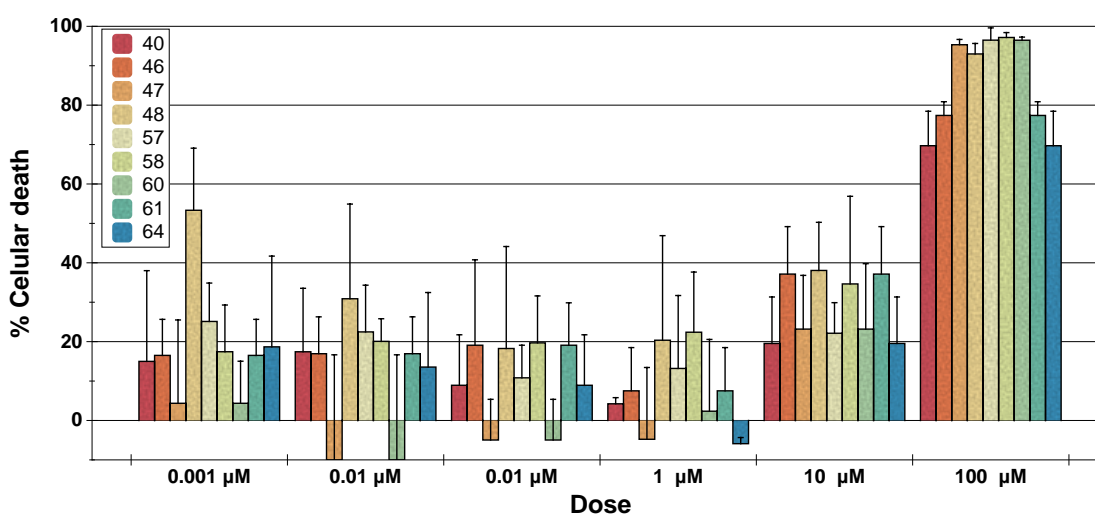

Figure 100. Toxicity of some triazine derivatives tested using the MTT assay.

4.4.6 In vivo evaluation of triazine 46.

With all the experiments performed up to the moment it could be concluded that triazine **46** is a uncompetitive TRPV1 blocker that acts as an open-channel inhibitor. It is selective against other selective and non selective calcium ion channels, like NMDA and TRPM8. Although it could not be definitively established, the Woodhull model suggested that triazine **46** binds from the extracellular side of the membrane to some site located relatively deep into the channel pore. The toxicity of triazine **46** is low in the MTT assay, suggesting a good therapeutic index.

To investigate the effects of **46** in living organisms, an in vivo evaluation was performed. Two common nociception and inflammation models were employed to this end. The hot plate test using bile ducted mice, and the Freund's adjuvant inflammatory test on mice paw.

4.4.6.1 Hot plate test.

The biological assay consists on locating the mice over a hot plate at 52 ºC and recording the time that the mice spent over the hot plate without licking its paw or jumping.[69] These are complex behaviors and are not spinally-mediated reflexes. Those measurements were recorded as paw withdrawal latency time (PWL). Longer time exposure to the plate without noticing the heat means that mice were not processing the painful signal and therefore were not feeling pain.

Triazine **46** was administered through an intraperitoneal injection at 10 mg/kg to a control group of mice (sham operated) and a group of mice whose bile duct had been ligated. Sham mice were prepared as a subject group that received an identical surgical procedure to the experimental group but without the treatment under study. The duct bile ligation (DBL) is considered a model of acute inflammation, making them more sensitive to temperature due to the over expression of TRPV1 among other factors. Firsts measures shown in Figure 101, (3 and 4 weeks old mice), represent the non treated mice of both sham and DBL group. As expected DBL group showed lower PWL values than sham group mice group. After injection of **46**, both groups showed an increase of PWL that is more accused in the BDL group. Indeed, PWL values for both sham and BDL group were comparable in the first 24 h period. The effect of **46** lasted for 96 h (4 days) after which the PWL measures recovered the initial untreated values (120 h).
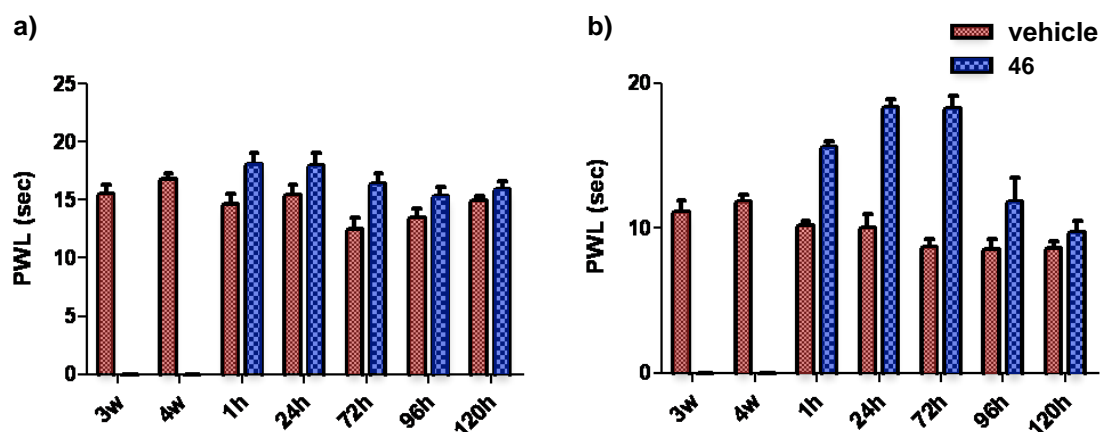
Figure 101. PWL recordings using the hot plate test for a) control mice (sham-operated mice), b) bile duct ligation (BDL) mice.

4.4.6.2 Freund's adjuvant test.

On Freund's adjuvant test an inflammatory cocktail is administered to mice paws. This inflammatory cocktail contains an antigen (1:1 oil/saline, 0.5 mg/mL, 50 µL) emulsified in mineral oil that produces an immune response of the organism, leading to inflammation and sensitization of the affected zone.[163] The variable measured is the number of scratches that the mouse performs on the affected zone. Less scratches means less inflammatory sensing activity on the treated paw and therefore an analgesic activity (Figure 102). In addition to accounting the scratches, a group of untreated mice where injected with Freund's adjuvant as a source of inflammation and then introduced in a hot plate with and without administration of **46** (10 mg/kg) to register the PWL response.

Both on scratches counting test and in the hot plate test using as pro-inflammatory factor the Freund's adjuvant the results were similar: Mice that had been treated with **46**, exhibit a less sensitive behavior than control mice in 1h and recovered the normal sensitivity after 120 hours. Thus, these experiments demonstrated the eficacy of triazine **46** as pain releaver and its low tocicity in animal models.
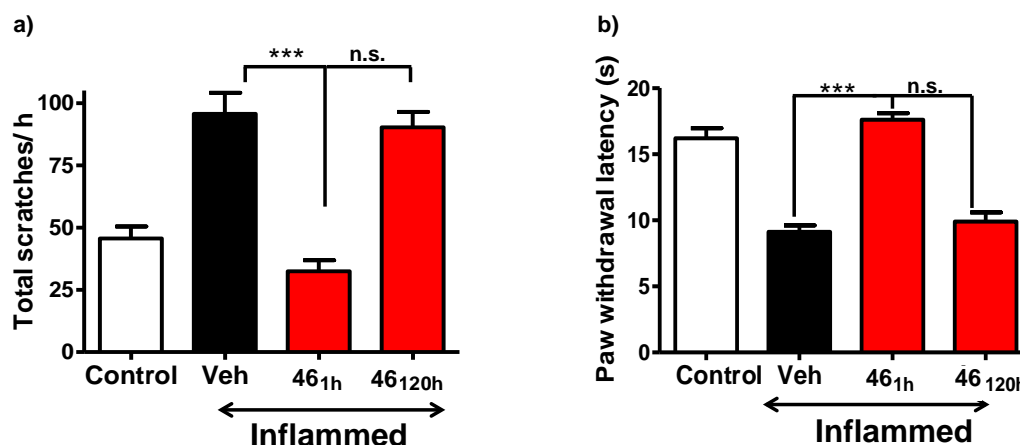
Figure 102. a) Inflammatory test using complete Freud's adjuvant. b) Hot plate test recordings for 1 and 120 h on mice treated with Freud's adjuvant. In both study cases the analgesic activity of **46** at 120 h is not significantly different from the vehicle control. *** P ≤ 0.001

4.4.7 Conclusions of the biological assays performed on triazine 46.

Triazine **46** was the most potent TRPV1 antagonist synthesized. It exhibited a very interesting mechanism, acting as an open channel blocker and being the most active non peptoid uncompetitive TRPV1 antagonist reported up to that moment.[147] In comparison with other uncompetitive reported products like methoctramine (IC_{50}(cap) = 2 μM[164]), the compound AG 489 isolated from the funnel spider (IC_{50}(cap) = 300 nM[149]) and ruthenium red (IC_{50}(cap) = 160 nM[164]), activity of compound **46** is several fold, or even more than one order of magnitude (if compared to methoctramine), more potent. In addition **46** acts as a polymodal blocker affecting both pH and capsaicin mediated evoked current while activity of ruthenium red is very sensitive to the pH. On the other hand methoctramine is known for being a muscarinic M2 receptor antagonist being less selective than **46**.

When compared with competitive TRPV1 antagonists, the activity of **46** can be located among the ten most potent blockers. Two of the most potent and developed TRPV1 competitive blockers AMG-517 (IC_{50} (cap) = 0.76 nM, IC_{50} (pH) = 0.63 nM, IC_{50}(45 ºC) = 1.3 nM) and SB-705498 (IC_{50} (cap) = 3 nM, IC_{50} (pH) = 80 nM, IC_{50} (45 ºC) = 6 nM) arrived to different phases of clinical trials. Having in mind the hit-to-lead process, compound **46** is just at the beginning of the process, having a good pharmacodynamic profile but mostly unknown pharmacokinetic properties. This data is what encouraged us to characterize the compound biological activity, toxicity and selectivity profile. Given the intial *in-vivo* results showing the potential of triazine **46** and

its possible use in sensitized systems, a patent was filed with the tittle "Triazine derivatives and their uses as TRPV1 inhibitors" in order to protect the discovery.[165]

Further development of triazines as TRPV1 blockers have to overcome issues like the common hyperthermia generated by most TRPV1 blockers, interaction with hERG channel, bioavailability, half life and clearance parameters, and blood brain barrier crossing.

Chapter 5 - 3D-QSAR study of the TRPV1 blockade activity.

The use of computational chemistry in medicinal chemistry helps to rationalize and assist the hit discovery process, the lead selection and optimization, and the design of new molecular entities. Moreover, it can help to modulate the physico-chemical properties of bioactive compounds in order to improve parameters like absorption, solubility and toxicity among others. Based on the available knowledge on the biological target these drug design methods are classically classified in two categories.

- Structure-based methods: those based on the known 3D-structure of the receptor.
- Ligand-based methods: those that rely on the structure of known ligands that bind to the biological target of interest.

Given the absence of structural information on TRPV1 and the difficulty to obtain accurate homology models due to its low homology (<20%) to other ionic channels with known structure, the ligand-based approach seemed the only option to quantitatively analyze the available SAR data on the newly synthesized TRPV1 antagonists, in order to obtain information that could help to predict the activity of new compounds.

A variety of ligand-based drug design methods have been described in the literature: molecular similarity approaches,[166] pharmacophore-based methods,[167] fingerprint-based methods,[168,169] classical quantitative structure-activity relationship (QSAR) analysis[170,171] and 3D-QSAR analysis,[172,173] among others. 3D-QSAR refers to the application of force field calculations requiring three dimensional structures, e.g. based on protein crystallography or molecule superimposition. 3D-QSAR methods are based on computed potentials, e.g. the Lennard-Jones potential, rather than experimental properties, and they are concerned with the overall molecule rather than a single substituent. Therefore, they require the calculation of different types of fields around the molecules which are dependent on their structure and conformation, like the molecular steric field (related to the shape of the molecule), the hydrophobic field (related to the water-soluble surface), or the electrostatic field (related to their capacity to establish polar interactions with the receptor).

Based on the previous experience of the group and on the availability of the required computational tools we decided to use two well established 3D-QSAR methodologies for our purposes: the Comparative Molecular Field Analysis (CoMFA)[174-

[176] and the Comparative Molecular Similarity Indices Analisis (CoMSIA) methods.[177-179] Both methods had previously been applied to the study of the TRPV1 antagonist activity of a collection of cinnamide derivatives.[180]

5.1 CoMFA and CoMSIA basics.

Despite the CoMFA and CoMSIA methods are implimented in the SYBYL sofware suite[181] and their application can be carried out in a mostly automatic manner, without requiring a direct manage of the calculations that are performed, a basic knowledge of the essential concepts of both methodologies is necessary to apply them properly. A brief description of these concepts is given in this section.

The idea underlying the CoMFA and CoMSIA methods is that the differences in a target property (e.g. biological activity) are related to the differences in the shapes of the non-covalent fields surrounding the tested molecules. Both methods derive from the molecular interaction field (MIF) concepts developed by Goodford and Cramer in the 80s.[172,175]

A most important precondition for the application of these methods is that all molecules have to interact with the same receptor in the same manner, i.e. with identical binding sites in the same relative geometry. Since all the products synthesized during this thesis had a highly similar structure, it was assumed that this condition was satisfied and that all of them would interact with the same channel region adopting a similar conformation. Thus, the hypothesis was that the most active products would share common structural features that allow to establish specific and strong interactions (hydrogen bonds, salt bridges, hydrophobic contacts,...) with the receptor, which translates into high activity, while the rest of the compounds would only be able to establish some of them and/or with less efficacy, which would translate into a lower activity.

From a practical point of view, for the calculation of the molecular fields, which are the basis of these methodologies, the molecules under study are placed in a 3D grid and a theoretical probe is moved through each grid point (node). Then, the interaction parameter (electrostatic or Van der Waals energies for CoMFA, or similarity indices for CoMSIA) between the molecule and the probe is calculated at each node. The matrix of values thus generated is the molecular interaction field (MIF), or, for the case of CoMSIA, the molecular similarity field (although here the term MIF will be used

indistinctly when talking about CoMFA or CoMSIA fields). To compare the fields of different molecules it is necessary that, previous to the calculation of the MIFs, they are aligned in a relevant disposition, and this is frequently the most important and difficult step in a CoMFA or CoMSIA study.
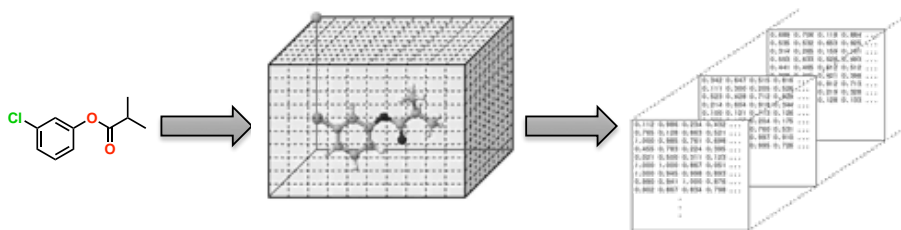

Figure 103. Molecule inside a grid showing the nodes where the probe is placed. The resolution of the grid box is determined by the step between two nodes. Evaluated interaction parameters are stored in n dimensional matrixes for further statistical analysis.

5.1.1 CoMFA Fields.

The CoMFA fields are derived from a theoretical probe that has the Van der Waals and electrostatic properties of an sp^3 carbon atom with a charge of +1. From the interaction with this probe, the steric and electrostatic CoMFA fields are calculated as Lennard-Jones (Equation *vi*) and Coulomb (Equation *vii*) potentials, respectively. To avoid large steric and electrostatic energies, all values exceeding a specified cut-off (by default 30 kcal/mol) are set to the cut-off value.

Equation (*vi*) $E_{vdW} = \sum_{i=1}^{n}\left(A_{ij}r_{ij}^{-12} - C_{ij}r_{ij}^{-6}\right)$

Equation (*vii*) $E_C = \sum_{i=1}^{n}\frac{q_i q_j}{D r_{ij}}$

Equations (*vi*) and (*vii*): A_{ij} and C_{ij} are constants that depend on the van der Waals radii of the atoms of the molecule and the probe; r_{ij} is the distance between atom *i* of the molecule and the grid point *j*; q_i and q_j are the partial charges of atom *i* of the molecule and of the probe; *D* is the dielectric constant.

5.1.2 CoMSIA Fields.

At variance with the CoMFA method that implies field descriptors based on the well established Lennard-Jones and Coulomb potentials, COMSIA uses arbitrary descriptors that reflect the spatial similarity or dissimilarity of molecules.[179] By means of a common probe atom, originally defined with a charge of +1, radius of 1 Å and hydrophobicity of +1, these similarity indices are calculated according to Equation (*viii*) at regularly spaced grid points for each compound in the data set. Therefore, they do

not exhibit a direct measure of similarity determined between all mutual pairs of molecules, but they rather evaluate the similarity of each molecule indirectly through the similarity to the common probe atom.

$$\text{Equation } (viii) \qquad A_{F,k}{}^{q}(j) = - \sum_{i=1}^{n} w_{probe,k} w_{ik} e^{-\alpha r_{iq}^{2}}$$

Equation (*viii*): $A_{F,k}{}^{q}(j)$ represents the similarity index between molecule *j* and the probe atom placed at grid point *q*; *i is* the summation index over all atoms of the molecule; w_{ik} and $w_{probe,k}$ are the actual values of the physicochemical property *k* for atom *i* and the probe atom; α is an attenuation factor; r_{iq} is the distance between the probe atom at grid point *q* and atom *i* of the test molecule.

A later development of the method modified the probe to include hydrogen-bond donor and acceptor properties of +1.[178] Thus, CoMSIA calculates five different types of similarity fields: steric, electrostatic, hydrophobic, H-bond donor and H-bond acceptor. These fields were selected to cover the major contributions to ligand binding.
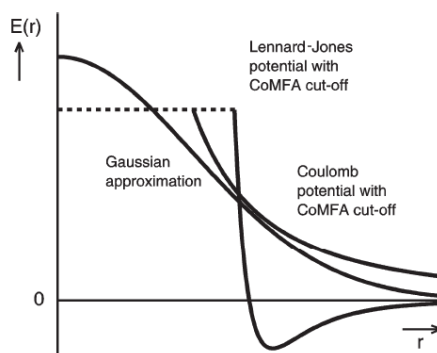
Figure 104. Shape of Lennard-Jones and Coulomb potentials used in CoMFA compared to the Gaussian-type function used in CoMSIA.[182]

In determining the CoMSIA similarity indices, the mutual distance between the probe atom and the atoms of the molecule is considered through a Gaussian type function. This eliminates the problems implicit in CoMFA, due to the use of Lennard-Jones and Coulomb potentials, of singularity points at the atom positions and the need to set up a cut-off to limit the large values in energy calculations (Figure 104). The shape of this Gaussian function is modulated by an attenuation factor (*α*). Large values of *α* will result in a strong attenuation of the distance-dependent consideration of

molecular similarity, resulting in little averaging of local feature matches of the molecules being compared, i.e. the global molecular similarity becomes less important. With small values of *α* also remote parts of each molecule will be experienced by the probe and the global molecular features become more important. The default value of *α*=0.3 permits a reasonable "local smearing" of the molecular similarity indices and helps to avoid extreme dependencies on small changes of the mutual alignments,[179] therefore it was used to calculate all CoMSIA fields in our study of the anti-TRPV1 activity.

The inclusion of a hydrophobic field in CoMSIA allows to take into consideration entropic contributions to binding, which are not taken into account in CoMFA as Coulombic and Lennard-Jones potentials solely describe the energetic contributions to the binding constants.[174] Representation of contour maps of the relative spatial contributions of the different fields to activity are useful tools for the interpretation of CoMFA and CoMSIA results. CoMFA field contributions highlights those regions in space where the aligned molecules would favorably or unfavorably interact with a certain environment, while the CoMSIA-field contribution denote those areas within the region occupied by the ligands that "favor" or "dislike" the presence of a group with a particular physicochemical property.[179]

5.1.3 Statistical techniques.

As previously mentioned, the results of a CoMFA or CoMSIA field calculation are matrices that usually contain thousands of columns, with field values (independent variables) that show a high internal correlation, and which must be correlated with a binding affinity or with other biological activity values (dependent variables). In order to extract a QSAR relationship from these high dimensional data matrices, correlation techniques that perform a reduction of the dimensionality are required.

5.1.3.1 Principal Component Analysis (PCA).

Principal component analysis (PCA) is a statistical procedure that uses an orthogonal transformation to convert a set of observations of possibly correlated variables into a set of values of linearly uncorrelated variables called principal components (PC). This transformation is defined in such a way that the first principal component has the largest possible variance, and each succeeding component in turn

has the highest variance possible under the constraint that it is orthogonal to (i.e., uncorrelated with) the preceding components. The enticing reason for using PCA in creating QSAR models is the ability to create compact and accurate models, minimizing the loss of information from the original data (molecular fields) while reducing the dimensionality of a signal, by determining a linear mapping to a smaller dimensional space.[183] In addition PCA analysis can allow the identification of compound clustering not obvious before the transformation.
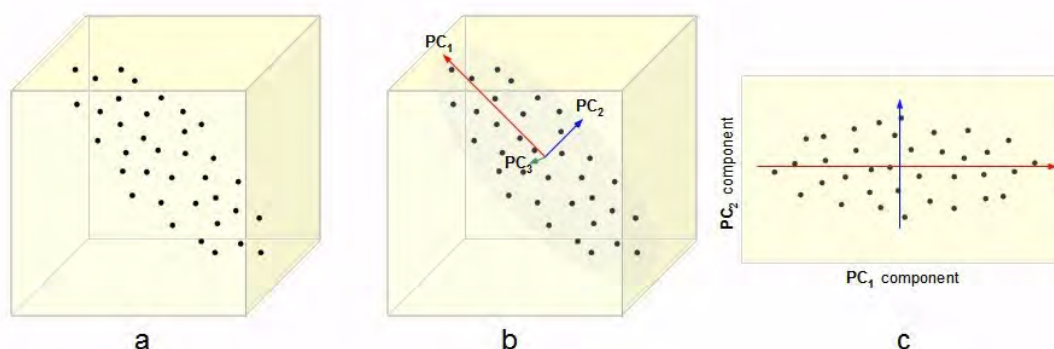

Figure 105. Illustration of principal component analysis of a 3D distribution of points (a) through selection of orthogonal components (b) and representation of the data using the two first components (c), thus reducing the original three dimensions to two (PC_1 and PC_2).

5.1.3.2 Partial Least Squares regression.

The use of principal components, rather than the original set of independent variables, to obtain a correlation with a dependent variable based on a standard linear regression model is known as Principal Component Regression (PCR). Tipically, the CoMFA and CoMSIA methods use the Partial Least Squares (PLS) regression, a statistical method that bears some relation to PCR. The fundamental difference between both methods is that in PLS analysis the orientation of the PLS components, or latent variables (also abreviated PC), does not exactly correspond to the orientation of the principal components. They are slightly skewed within their confidence hyperboxes, in order to achieve a maximum intercorrelation with the independent variables.[182] SAMPLS (SAMple-distance PLS)[184] is a modification of the PLS analysis where the latent variables are derived from the covariance matrix. Although SAMPLS has no major advantage relative to PLS, it operates much faster than the standard PLS algorithm and therefore its use is recommended whenever is possible.

5.1.3.3 Validation methods.

Once a PLS model is constructed from a set of compounds, i.e. the *training set*, a validation should be carried out in order to assess the ability of the model to make predictions. The sole measure of the goodness of fit of the model (r^2) is no criterion for its validity or predictive capacity. Indeed, models that are built with a high enough number of latent variables can show an almost perfect correlation ($r^2 \sim 1$) but a null capacity to make predictions, a situation known as *overfitting*.

Internal validation through cross-validation is the first approach to judge the validity of the PLS model and the significance of additional PLS latent variables included in the model. In the most common leave-one-out (LOO) cross-validation, one object (i.e., one compound) is eliminated from the training set and a new reduced PLS model is derived from the residual compounds. This model is used to predict the biological activity value of the compound that has been removed. The same procedure is repeated until all objects have been eliminated once. The sum of the squared differences between these 'outside-predictions' and the observed y values, PRESS = $\sum (y_{pred} - y_{obs})^2$, is a measure for the internal predictivity of the PLS model. For large data sets, where all or most objects have close neighbors in multidimensional parameter space, LOO is a too optimistic validation method. In those cases, an alternative to the LOO technique, i.e., leave-several-out (LSO), is recommended to yield more stable PLS models: Several objects are eliminated from the data set at a time, randomly or in a systematic manner, and the excluded objects are predicted by the corresponding reduced model.[173]

In cross-validation, a q^2 (r^2_{PRESS}) value is defined like the r^2 in regression, but using PRESS instead of the unexplained variance (Figure 106). Cross-validated q^2 values are always smaller than the r^2 values including all objects. As long as only significant PLS components are included to build the model, q^2 increases, whereas decreasing q^2 values indicate inclussion of non-significant components, i.e. overfitting. Thus, at the extremes, a value of $q^2=1$ would correspond to perfect predictions, while a value of 0 would imply that there is no model at all, i.e., the predictions would be no more accurate than taking the average target property value of all the tested compounds. From a practical point of view, a general rule-of-thumb suggests that q^2 values above 0.6 (LOO, or > 0.5 if LSO) mean a significant predictivity of the QSAR model while values lower than 0.4 mean poor predictivity.[185] Another practical rule suggests that additional PLS components should be considered for inclussion in the

model only as long as they represent an increase of at least 5% in the q^2 value. An additional criterion to decide which is the optimum number of PLS latent variables is the Standard Deviation of the Error of Predictions (SDEP): The smallest SDEP value dictates this optimum number. Figure 106 resumes the process to perform the cross-validation and decission on the optimum number of PLS components when generating a CoMFA or CoMSIA QSAR model.

Other internal validation methods, like bootstrapping or scrambling,[182] can also be used to asses the significance and robustness of the QSAR model. However, it is commonly accepted that the most definitive method of validation is by making a correct prediction of the target property or activity of an external set of compounds not used in developing the model, i.e. the *test set.* [186]
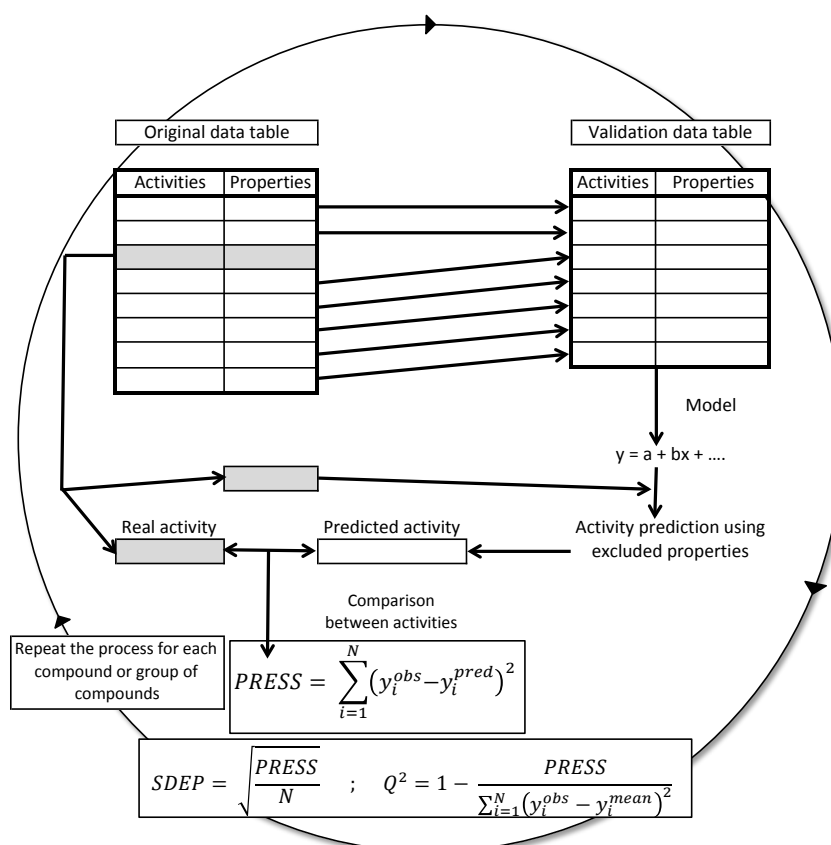

Figure 106. Cross-validation process: the grey area on the original data table represents one or more rows (compounds) being removed for the cross-validation evaluation.

5.1.4 Selection of training and test sets.

Selection of proper training and test sets is an important step in any QSAR study, although it has often been neglected. In such cases, problems can arise from a

biased object selection or from different structural and parameter spaces of the training and test sets.[182] Different selection methods can be used when there is a high enough number of objects to ensure a random and representative selection of training and test compounds, however this is more difficult when the total number of compounds is smaller, i.e. a few dozens. The training set compounds should span a parameter space in which all data points are more or less equally distributed. The structures and all relevant properties of the test set compounds should not be too far from the training set compounds. To derive statistically significant models, an appropriate design scheme should be used to cover the property space with the smallest possible number of objects. Redundancy is minimized by following this recommendation, however some redundancy should be included to avoid the possibility that cross-validation is no longer applicable and that single point errors distort the final QSAR model. Reasonable results for the test set predictions can only be expected by including sufficient redundancy in the training set compounds.[182]

5.2 Construction of the 3D-QSAR model.

5.2.1 Selection of compounds.

In order to generate a statistically significant QSAR model it is desirable that a relatively large amount of structurally diverse compounds, with known activity and which interact with the same binding site of the biological receptor, are available. The activity of those compounds should cover several orders of magnitude (>3) and they should be distributed homogenously over that range. Finally, it is desirable that the active conformation of some of the most active compounds is known (from crystallography, computational docking…) or that they present a relatively rigid structure that allows to make a reliable predicton about what this active conformation may be. This active conformation is required to establish an aligment criteria for all the compounds in the data set.

At the point when the present study was carried out, there were only 35 trisubstituted triazines (**17**, **40-48**, **50-74**) plus the two original peptoid hits (**D161515** and **D191515**) that had been synthesized and evaluated to determine their potency (IC_{50}) in a consistent manner by our group. As has been shown in the previous chapter, the activity of these compounds covered more than 6 orders of magnitude and their distribution over that range was reasonably homogeneus, except for the less active region (Figure 107).
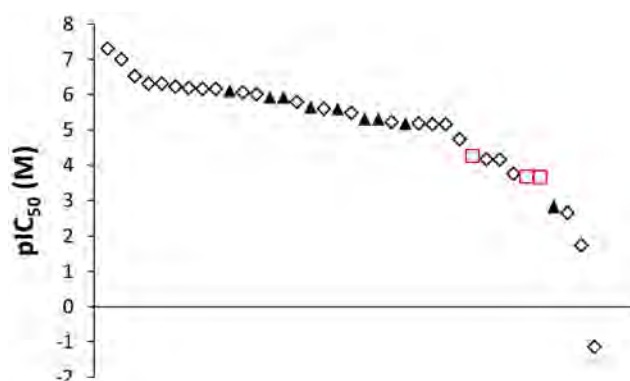
Figure 107. Distribution of the activities (expresed as pIC_{50} = -$logIC_{50}$ (M)) of the full set of compounds considered to carry out the 3D-QSAR analysis. Values for the training set compounds (empty diamonds), test set compounds (black triangles) and identified outliers (red squares) are shown. Classification of the compounds in each of these 3 groups will be justified in the following sections.

Concerning their structure, most of them were highly flexible (e.g. the most active triazine, **46**, has >10 rotatable bonds) and, due to the lack of structural information about the receptor, it was difficult to make hypothese about the active conformation of any of them. However, from the previously described SAR data (Chapter 4) some clues about their mode of interaction could be extracted:

- The evaluated triazines interact with TRPV1 exhibiting a uncompetitive behavior,[147] which suggests that they do not bind at the capsaicin site.
- The mode of action of the most active triazine **46** points in the direction that it interacts from the extracellular side of the channel, and relatively deep in the aqueous pore of TRPV1,[147] similarly to quaternary substituted ammonium cations like tetraethylammonium.[187]
- Most of the synthesized triazines are positively ionized under physiological conditions.

Those facts led to hypothesize that at least some of the synthesized triazines could interact with the negatively charged vestibule of the TRPV1 pore, or even place their alkylic chain with a cationic end-group (e.g. protonated dimethylamino) inside of the pore, whose structure is designed to allocate cations (ie. Ca^{2+}, K^+,…), while the rest of the molecule stays in the vestibule. Indeed, based on a temptative homology model of the TRPV1 channel, a preliminary binding model of triazine **46** showed that the dimethylaminopropyl moiety could fit into the pore, establishing polar interactions with

several of its residues (Figure 108). This binding model would occur from the extracellular side of the channel and it would be compatible with the experimentally estimated depth of binding. Similar binding modes could be postulated for other triazine antagonists that share in common with **46** the presence of a dimethylaminoalkyl moiety in their structure, therefore a putative active conformation was proposed based on the T-shaped conformation of **46** shown in Figure 108. This conformation was considered as a posible template to perform the aligment of the rest of the compounds.
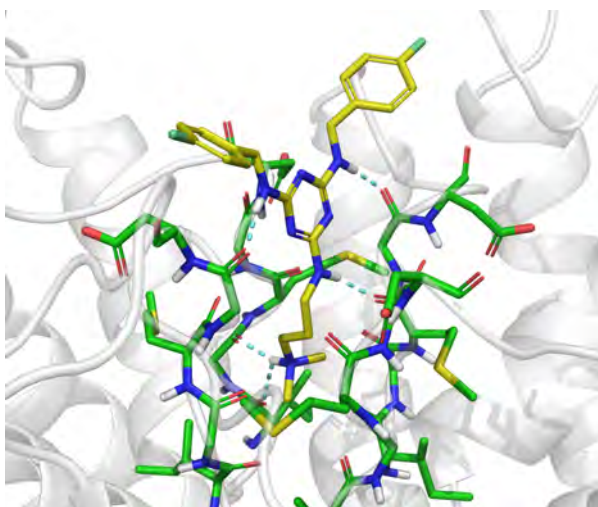
Figure 108. Binding model of the selectivity filter of human TRPV1 blocked by triazine **46**. The homology model of the TRPV1 channel was built based on the structure of Kv1.2 (PDB 2A79)[33,188,189] and it is limited to the S5-S6 fragment (residues 574-688), omitting a 19-residues loop (residues 610-628) that could not be modeled since it is not present in the structure of Kv1.2. Compound **46** is shown in yellow with its dimethylaminopropyl moiety inserted into the pore. The protonated dimethylamino and the triazine attached amino groups are shown forming hydrogen bonds with residues of the protein, namely Gly644, Met645 and Gly646.

In the conformation shown on Figure 108, the phenyl rings of **46** lie aproximately parallel to the vestibule of the channel, without establishing clear interactions with the residues of the protein. This could be an artifact of the homology model, which lacked a 19-residues fragment which contains some aromatic residues that could interact with that part of the ligand. For this reason, a search among the structures of the active compounds was performed to find more rigid structures that could provide an alternative criteria for alignment, particularly for the aromatic side chains. That was the case of triazine **72**, which includes a tetrahydropyridoindolyl moiety instead of the more flexible fluorophenethyl group present in **46**.

Figure 109. Structures of the active triazines chosen as templates.

5.2.2 Preparation of structures and alignment.

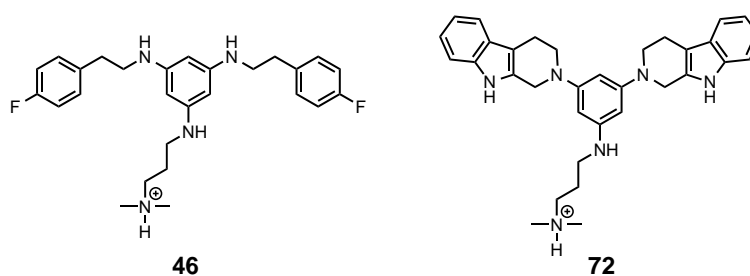Triazines **46** and **72** were selected as templates to carry out the aligment of the rest of the molecules. The bound conformation of **46**, shown in Figure 108, was the first template and it was used to also define a conformation for **72** in which the dimethylaminopropyl moiety held a similar extended disposition, required to get into the TRPV1-pore, but its other two policyclic side chains adopted a minimum energy conformation. All the other triazine structures that included at least one tertiary amino group, as well as the two original peptoid structures (**D161515** and **D191515**), were modeled in the monoprotonated state. Triazines with more than one protonable amino group were modeled with the charge on the most basic amino group, according to their calculated pK_a (see Annex 3). Triazines with no protonable group were modeled in the neutral state. All compounds were assigned partial charges and energy minimized with the MMFF94x force field,[190-192] previous to be aligned on the respective templates. For the alignment, first the triazine ring of every compound was manually prealigned with the triazine ring of **46** or **72**, in a disposition where the side chains were properly oriented towards the homologue side chains of the templates (i.e. aromatic on aromatic and cationic on cationic side chains). The two peptoids were also manually superimposed on the templates starting from the cationic group and using the corresponding side chains to achieve a reasonable initial alignment. Then, an automatic alignment software, the Flexible Alignment (FlexAlign) module included in the Molecular Operating Environment (MOE) Suite,[193,194] was used to improve the alignment and overlap of each structure on the corresponding template, while the later was kept rigid. FlexAlign parameters were adjusted to maximize the superposition of relevant features such as aromatic rings, hydrophobic moieties, hydrogen bond donors and acceptors, and molecular volume, while minimizing the internal strain. The

resulting structures were checked one by one and manually adjusted, if required, to maximize the superposition to the template. To finish, a further refinement of the two alignments was carried out with FlexAlign. These two alignments, Alignment 1 from triazine **46** and Alignment 2 from triazine **72**, are shown in Figure 110.
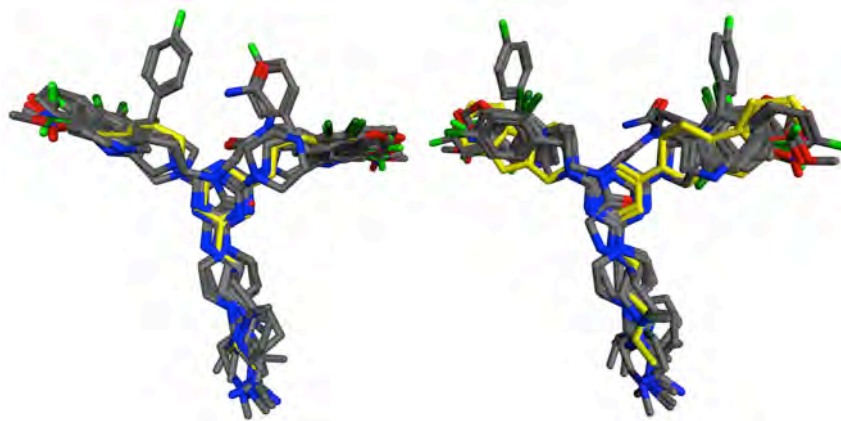
Figure 110. Structural alignments of all the compounds considered for the 3D-QSAR study on the template conformations of **46** (left, Alignment 1) and **72** (right, Alignment 2). Templates are colored in yellow.

5.2.3 MIFs of triazines 46 and 72.

The resulting aligned conformations of each molecule were loaded in two tables in the program SYBYL[181] and CoMFA and CoMSIA MIFs were generated for each molecule as starting point to build the 3D-QSAR models. Different grid spacings (2.0, 1.0 and 0.5 Å) were selected to check their effect on the CoMFA and CoMSIA models. Smaller spacings give more resolution and smother field shapes but they result on larger calculation times. 3D-contour maps are usually used to obtain a graphical representation of the MIFs for each molecule. These contour maps are isosurfaces conecting points in 3D space which have the same field value. The contour-level to be plotted is normally selected through a percentile of the overall range of values within the field.

5.2.3.1 CoMFA MIFs.

Both steric and electrostatic COMFA MIFs were generated using the default SYBYL parameters except for the grid spacing. The steric and electrostatic COMFA fields for both templates, **46** and **72**, are shown in Figures 111 and 112.

Figure 111. CoMFA steric MIFs of templates **46** (left) and **72** (rigth), at 0.5 Å grid resolution and contoured at 95 (green) and 5 % (yellow).

The CoMFA steric MIF represents the van der Waals interaction potential between the probe and the molecule and it also provides information about the volume occupied by the molecule. Both green and yellow surfaces in Figure 111 represent different isocontour levels: the yellow contours indicate regions of negative steric potential while the green contours indicate regions of positive steric potential.

Figure 112. CoMFA electrostatic MIFs of templates **46** (left) and **72** (rigth), at 0.5 Å grid resolution and contoured at 95 (blue) and 1 % (red).

The electrostatic MIF represents the Coulomb potential between the probe and the molecule, which bears atom-centered point charges. The blue contours in Figure 112 indicate regions of positive electrostatic potential while the red contours indicate regions of negative electrostatic potential. In accordance with this, the blue contours are centered around the positively charged dimethylammonium groups of triazines **46** and **72**, while the red contours are located around the aromatic rings and the triazine rings.

It is noteworthy that the steric and electrostatic CoMFA MIFs appear only outside of the molecules, i.e. out of the Van der Waals radii of its atoms. This is because, as has been already mentioned (section 5.1.2), the value of the potentials at

the grid nodes that are closer to the atoms of the ligands tend to be very large due to repulsive steric and repulsive/atractive electrostatic forces (Figure 104), therefore they are limited by default to a cut-off value of 30 kcal/mol.

5.2.3.2 CoMSIA MIFs.

At variance with the above, the fact that a Gaussian function, rather than Coulomb or Lennard-Jones potentials, is used to generate the CoMSIA MIFs results in smother fields that can be found even inside of the volume occupied by the molecule. This is because no "in molecule cut-off" is defined. In addition the attenuation factor α (preset at 0.3) present in the similarity function regulates the distance dependence of the similarity function.

As in CoMFA, the CoMSIA steric MIFs reflect the shape of the molecules (Figure 113) by determining the similarity of their atoms with the probe. Thus, contours shown in green in Figure 113 correspond to regions which are more similar to the probe while those in yellow correspond to regions which are more dissimilar.
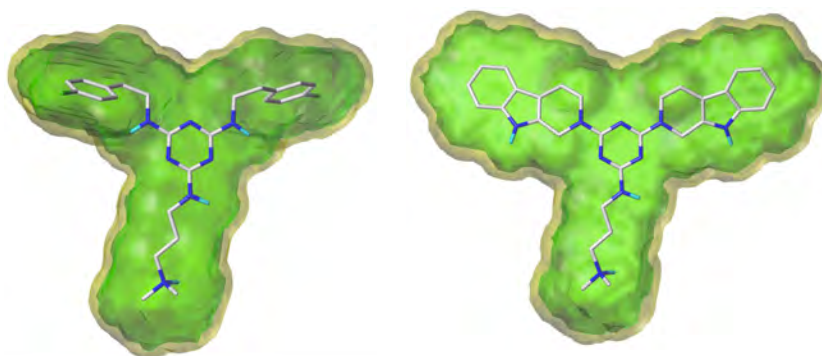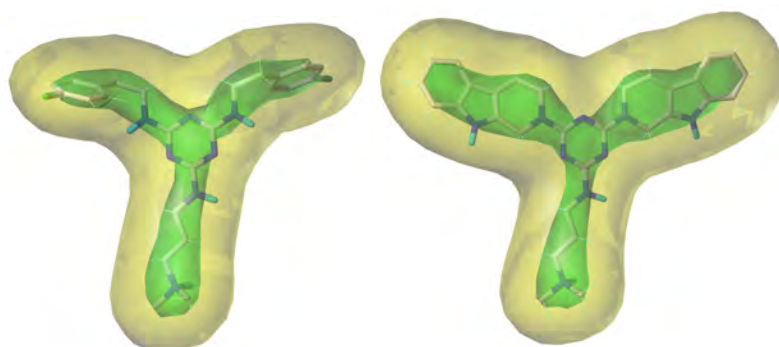

Figure 113. CoMSIA steric MIFs of templates **46** (left) and **72** (rigth), at 1.0 Å grid resolution and contoured at 80 (green) and 20 % (yellow).

Similarly, the CoMSIA electrostatic MIFs evidence the aromatic rings electronic density, in red, and positive regions near the charged dimethylammonium group, in blue (Figure 114). It is noticeable how the aromatic and fluoride atoms of triazine **46** are well mimicked by the extended aromatic ring of molecule **72**. It is remarkable too that although the space disposition of the aromatic rings is different, the volume occupied by the electrostatic MIFs for both molecules are similar. In comparison with the CoMFA electrostatic fields shown on Figure 112, here the negative surface areas are located along the aromatic ring and not on top of it and the fluoride atom has a smaller impact in the whole negative region.
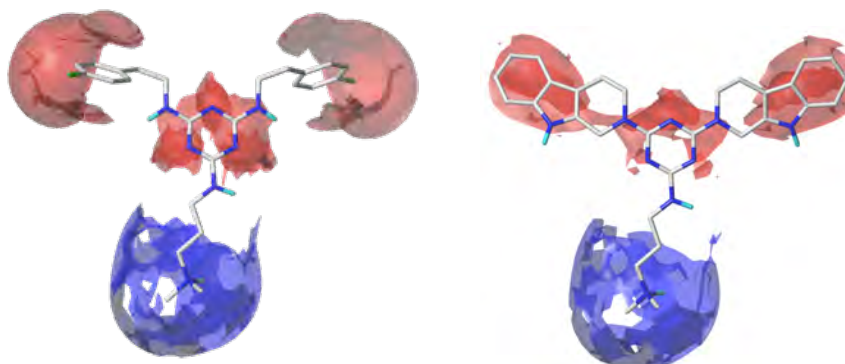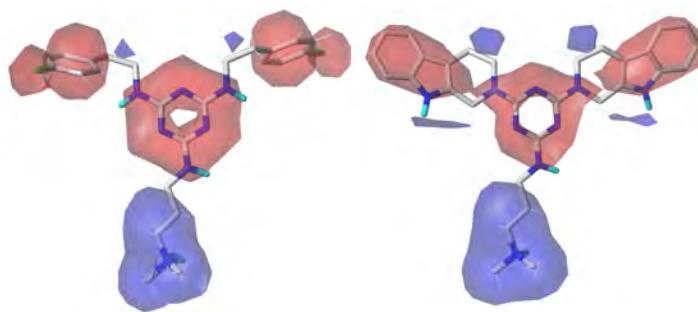
Figure 114. CoMSIA electrostatic MIFs of templates **46** (left) and **72** (rigth), at 1.0 Å grid resolution and contoured at 80 (blue) and 20 % (red).

The CoMSIA hydrophobic MIFs of templates **46** and **72** exhibit the highest similarity indices (yellow surfaces) near the aromatic regions (Figure 115). At a lower contour level (gray surfaces) this hydrophobic regions extent further around the molecules, except where the more polar NH groups are located.
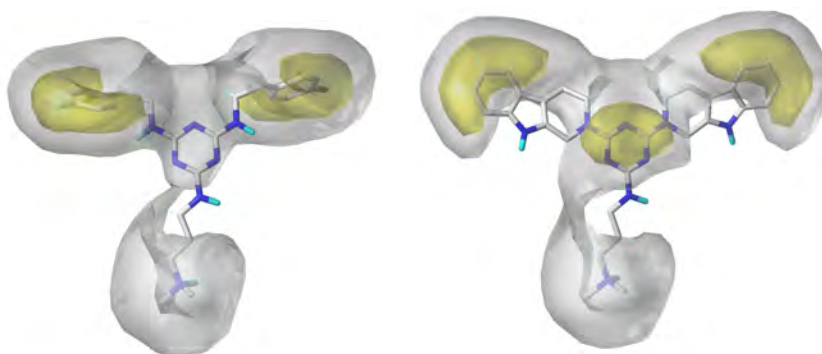
Figure 115. CoMSIA hydrophobic MIFs of templates **46** (left) and **72** (rigth), at 1.0 Å grid resolution and contoured at 80 (yellow) and 40 % (gray).

The hydrogen-bond donor CoMSIA field describes where hydrogen bond acceptor groups should be located on the receptor to establish a H-bond interaction. Accordingly, they are centered next to the NH groups of triazines **46** and **72**, as shown in Figure 116. Similarly, the hydrogen-bond acceptor field contains information about where hydrogen bond donating groups should be located on the receptor to establish such kind of interaction. The strongest acceptor field regions are located close to the nitrogens of the triazine rings of **46** and **72** (Figure 117).
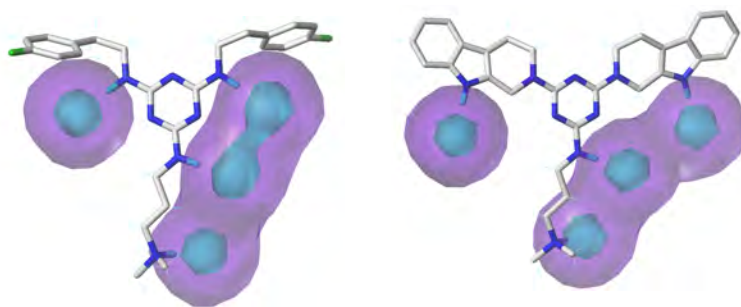
Figure 116. CoMSIA donor MIFs of templates **46** (left) and **72** (rigth), at 1.0 Å grid resolution and contoured at 80 (cyan) and 20 % (purple).
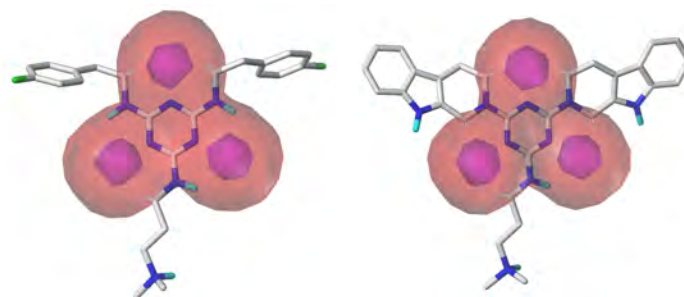

Figure 117. CoMSIA acceptor MIFs of templates **46** (left) and **72** (rigth), at 1.0 Å grid resolution and contoured at 80 (magenta) and 20 % (red).

5.2.4 Preliminary 3D-QSAR models.

An initial rapid screening including the full set of compounds (triazines **17**, **40-48**, **50-74**, and peptoids **D161515** and **D191515**, 37 compounds in total) as training set was performed to generate different preliminary 3D-QSAR models, in order to check what combination of conditions (alignment, field type, number of latent variables,...) could lead to statistically significant models.

Table 11. Statistical data for preliminary QSAR models using the full set of 37 compounds. Only the results for the optimum number of components, according to the leave-one-out method, are shown. [a] Leave-one-out q^2. [b] Leave-one-out predictive error sum of squares. [c] Number of PLS components.

Model	Alignment	q^2 (LOO)[a]	PRESS (LOO)[b]	N[c]	Field type
preCOMFA-1	1	0.02	1.62	1	Ster./Electr.
preCOMFA-2	2	0.03	1.61	1	Ster./Electr.
preCoMSIA-1	1	0.20	1.50	3	Steric
preCoMSIA-2	1	0.17	1.49	1	Electrostatic
preCoMSIA-3	1	-0.19	1.78	1	Hydrophobic
preCoMSIA-4	1	0.48	1.23	4	Donor
preCoMSIA-5	1	-0.05	1.68	1	Acceptor
preCoMSIA-6	2	0.21	1.50	3	Steric
preCoMSIA-7	2	0.15	1.51	1	Electrostatic
preCoMSIA-8	2	-0.19	178	1	Hydrophobic
preCoMSIA-9	2	0.41	1.31	4	Donor
preCoMSIA-10	2	-0.09	1.71	1	Acceptor

Thus, using fields generated with 2.0 Å grid spacing, the PLS analysis showed that the combination of both the steric and electrostatic CoMFA fields led to models with very low predicivity ($q^2 \sim 0$, see Table 11). Using the CoMSIA fields the results were better, particularly for models generated from the donor fields (preCoMSIA-4 and preCoMSIA-9, derived from Alignment 1 and 2, respectively) which showed a $q^2 > 0.4$.

Examining the structures of the compounds considered and how could they affect the results of the 3D-QSAR models, it was concluded that at least three of them could be recognized as outliers, i.e. compounds whose structures include features not present in any other compound among the full set. These compounds were triazines **70**, **73** and **74**:

- **70** was the only triazine capable to achieve a total charge of -2 under physiological conditions due to the presence of two aromatic carboxylic acid groups and no protonable group.
- **73** was the only triazine presenting two bulky moieties of N-(bisphenylmethyl)piperazine instead of the two aromatic rings present in most of the other compounds considered.
- **74** was the only compound presenting two cyclohexenyl rings instead of the aromatic rings present in most of the other compounds considered.

As previously mentioned (Section 5.1.4), the presence of these compunds in the training set could distort the statistics since, when they are removed during the LOO validation, the corresponding reduced models would not be able to predict their activities accurately. Removal of these three compounds from the training set led to a general improvement of the LOO statistics (Table 12). In particular, CoMSIA models derived from the donor field (preCoMSIA-14 and preCoMSIA-19, derived from Alignment 1 and 2, respectively) achieved q^2 values above 0.6, suggesting a significant correlation with the experimental biological activity of this collection of compounds. The correlation with the CoMSIA electrostatic and steric molecular fields were less significant but they achieved q^2 values around 0.3, whilst both hydrophobic and acceptor fields appeared as not being correlated with activity since they presented negative q^2 values.

144

Table 12. Statistical data for preliminary QSAR models using the full set except outliers **70**, **73**, **74** as training set. Only the results for the optimum number of components, according to the leave-one-out method, are shown. [a] Leave-one-out q^2. [b] Leave-one-out predictive error sum of squares. [c] Number of components.

Model	Alignment	q^2 (LOO)[a]	PRESS (LOO)[b]	N[c]	Field type
preCOMFA-3	1	0.29	1.40	1	Ster./Electr.
preCOMFA-4	2	0.29	1.40	1	Ster./Electr.
preCoMSIA-11	1	0.33	1,41	3	Steric
preCoMSIA-12	1	0.39	1.38	5	Electrostatic
preCoMSIA-13	1	-0.11	1.75	1	Hydrophobic
preCoMSIA-14	1	0.64	1.05	5	Donor
preCoMSIA-15	1	-0.11	1.75	1	Acceptor
preCoMSIA-16	2	0.24	1.50	3	Steric
preCoMSIA-17	2	0.34	1.39	3	Electrostatic
preCoMSIA-18	2	-0.27	1.88	1	Hydrophobic
preCoMSIA-19	2	0.61	1.11	5	Donor
preCoMSIA-20	2	-0.11	1.75	1	Acceptor

Although the statistical LOO parameters for the correlations using the CoMSIA donor MIFs were reasonable (Table 12), it was decided to perform a more in depth PLS analysis, with a more robust internal validation and a test set validation, to try to obtain 3D-QSAR models with predictive capacity. After outlier removal, the number of compounds was reduced to 34. Due to this small number, random selection of compounds to constitute non-biased training and test-sets was discarded and therefore a group of compounds were selected manually according to their structural features, attempting to select only those that were sufficiently represented in the remaining group of compounds, to allow that the 3D-QSAR could capture most of the chemical diversity present in the full collection.

Compounds included in the training set (**TRS**, 25 compounds) were **DD-161515**, **40**, **43**, **44**, **45**, **46**, **47**, **48**, **50**, **51**, **52**, **53**, **55**, **56**, **57**, **58**, **59**, **60**, **61**, **62, 65**, **66**, **68**, **69** and **72**. On the other hand the test set (**TES**, 9 compounds) was composed by products **DD-191515**, **17**, **41**, **42**, **54**, **63**, **64**, **67** and **71**.

These two sets (**TRS** and **TES**) of previously aligned compounds were employed to build and validate new PLS-derived 3D-QSAR models. Table 13 summarizes the statistical parameters of these new models. Comparison with the results of Table 12 shows that the models generated from the new training set in general are not worse than those obtained with the larger set of compounds. The most relevant change was observed in the statistics of the models derived from the CoMSIA electrostatic fields which now reached the threshold of $q^2 > 0.4$ with both alignments

(pre-ComSIA-22 and -27). On the other hand, the CoMFA derived models and those derived from the CoMSIA steric, hydrophobic or acceptor fields still showed little or no significance, i.e. $q^2 < 0.3$.

Table 13. Statistical data for preliminary QSAR models using the **TRS** training set. Only the results for the optimum number of components, according to the leave-one-out method, are shown. [a] Leave-one-out q^2. [b] Leave-one-out predictive error sum of squares. [c] Number of components.

Model	Alignment	q^2 (LOO)[a]	PRESS (LOO)[b]	N[c]	Field type
preCOMFA-5	1	0.22	1.65	1	Ster./Electr.
preCOMFA-6	2	0.20	1.67	1	Ster./Electr.
preCoMSIA-21	1	0.3	1.65	3	Steric
preCoMSIA-22	1	0.46	1.51	5	Electrostatic
preCoMSIA-23	1	-0.09	2.15	5	Hydrophobic
preCoMSIA-24	1	0.66	1.17	4	Donor
preCoMSIA-25	1	-0.13	2.04	2	Acceptor
preCoMSIA-26	2	0.27	1.67	3	Steric
preCoMSIA-27	2	0.42	1.50	3	Electrostatic
preCoMSIA-28	2	0.19	1.86	5	Hydrophobic
preCoMSIA-29	2	0.58	1.30	4	Donor
preCoMSIA-30	2	-0.15	2.01	1	Acceptor

As a final preliminary test to determine the best conditions to build statistically robust 3D-QSAR models, the influence of the grid spacing on their quality was evaluated. For that purpose, only the most relevant donor and electrostatic CoMSIA fields, calculated with different grid spacings of 2, 1 and 0.5 Å, were used to generate new models, and their statistical parameters are shown in Table 14.

Table 14. Statistical data for preliminary QSAR models using the **TRS** training set and fields generated with different grid spacings. Only the results for the optimum number of components, according to the leave-one-out method, are shown. [a] Leave-one-out q^2. [b] Leave-one-out predictive error sum of squares. [c] Number of components.

Model	Alignment	Grid Space Å	q^2 (LOO)[a]	PRESS (LOO)[b]	N[c]	Field type
preCoMSIA-31	1	2	0.66	1.170	4	Donor
preCoMSIA-32	1	2	0.40	1.52	3	Electrostatic
preCoMSIA-33	1	1	0.65	1.192	4	Donor
preCoMSIA-34	1	1	0.41	1.506	3	Electrostatic
preCoMSIA-35	1	0.5	0.65	1.19	4	Donor
preCoMSIA-36	1	0.5	0.41	1.51	3	Electrostatic
preCoMSIA-37	2	2	0.58	1.30	4	Donor
preCoMSIA-38	2	2	0.42	1.50	3	Electrostatic
preCoMSIA-39	2	1	0.58	1.33	5	Donor
preCoMSIA-40	2	1	0.43	1.55	5	Electrostatic
preCoMSIA-41	2	0.5	0.57	1.31	4	Donor
preCoMSIA-42	2	0.5	0.43	1.55	5	Electrostatic

The results showed that reducing the spacing, i.e. increasing the resolution, of the grid did not result in any significant change in the statistics of the models. Since decreasing the spacing of the grid leads to longer computation times without any apparent benefit in terms of predictivity, it was decided to conduct the rest of these studies using a grid step of 2 Å.

5.2.5 Construction and validation of 3D-QSAR models.

After the preliminary screening with CoMFA and CoMSIA MIFs and realizing the possible relevance of each one, a total of 18 3D-QSAR models were constructed. Each MIF combination was tested with both Alignments 1 and 2. The models generated for each alignment used CoMFA with both electrostatic and steric fields combined (CoMFA-1 and -2), and CoMSIA with steric, electrostatic and donor fields alone or in combination (CoMSIA-1 to -16). As models were generated, random groups cross-validation was performed to further assess the robustness and statistical confidence of the best models. This cross-validation was carried out using 10 groups, i.e. 10 random groups are generated and each one is removed once to perform the cross-validation, and this was repeated for 10 times. The average statistical values of q^2 and PRESS (q^2 (CV) and PRESS (CV), respectively), as well as the predictions for the test set, were used as criteria to decide about the quality of the models (see Tables 15 to 17 and Figures 122 to 124 at the end of this chapter).

The best statistical results were obtained using Alignment 1 considering the donor field alone (CoMSIA-4: q^2 (CV) = 0.65, PRESS (CV) = 1.19, r^2 = 0.88, 4 PC) or in combination with the electrostatic field (CoMSIA-7: q^2 (CV) = 0.60, PRESS (CV) = 1.27, r^2 = 0.96, 4 PC). Models from Alignment 2 showed slightly worse statistics, being the best one built from a combination of the donor and electrostatic fields (CoMSIA-15: q^2 (CV) = 0.57, PRESS (CV) = 1.32, r^2 = 0.95, 4 PC) (Table 15). It was noticed that the q^2 values obtained either by the LOO or LSO methods were in good general agreement, confirming LOO as a useful and fast preliminary screening method. Concerning the test set, predictions with model CoMSIA-4 showed a reasonable correlation with r^2 = 0.88, identical to the r^2 value obtained for the training set. CoMSIA-7 and -15 produced slightly worse results, with r^2 = 0.79 and 0.73, respectively, which are below the values for the training set, thus suggesting some overfitting in these models. Predictions for the three triazines previously discarded as outliers were clearly worse than those for

the test set, confirming that they cannot be considered within the applicability domain of these models.
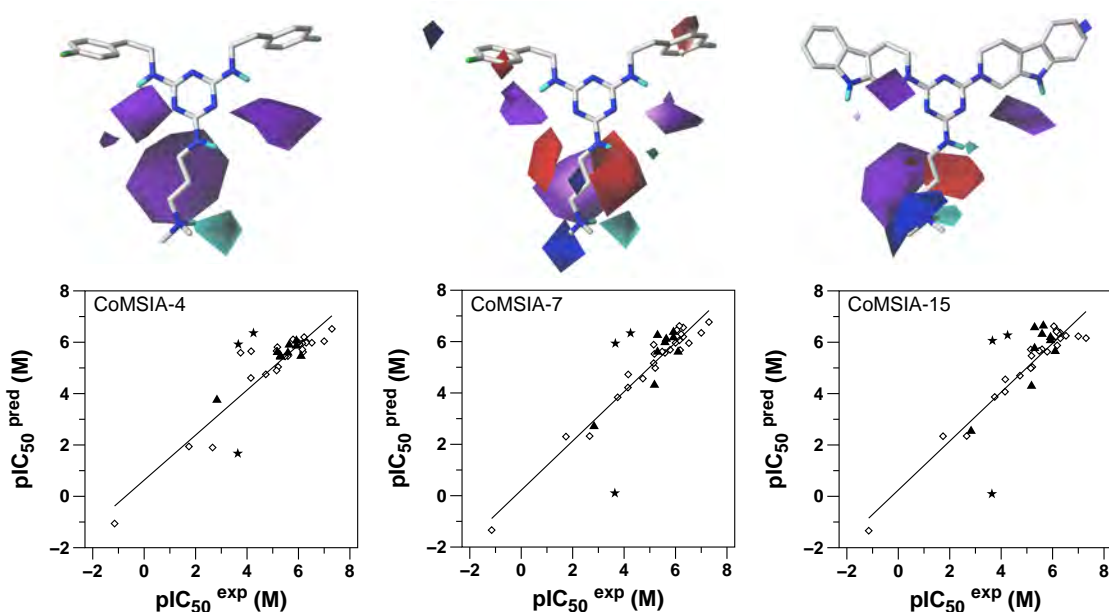
Figure 118. Top: CoMSIA isocontour maps (standard StDev*Coeff representation) contoured at 80 (cyan and blue) and 20 % (purple and red) for the most statistically relevant models, superposed on the corresponding template triazines (**46** for ComSIA-4 and -7, and **72** for CoMSIA-15). Bottom: Predicted vs. experimental pIC_{50} correlations; products are represented as: Training set (◊), Test set (▲) and Outliers (★). CoMSIA-4 was derived exclusively from donor field contributions (contours cyan and purple), while CoMSIA-7 and -15 also included contributions from the electrostatic field (contours blue and red). Cyan and blue polyhedra represent "favored" contour levels while purple and red polyhedra represent "disfavored" contour levels. Thus, the cyan and blue regions are those where the presence of a donor or a positive charge in the ligand (or an acceptor or negatively charged group on the receptor) increase the activity, while the purple and red regions are those where the presence of a donor or a positive charge in the ligand decrease the activity.

5.2.6 Interpretation of 3D-QSAR models.

Examination of the contribution of each field to activity is useful to rationalize the activities determined for each compound and to suggest modifications on the ligand structures to improve them. Representation of the StDev*Coeff contours from the PLS is the standard way of viewing the output of CoMFA or CoMSIA analyses. It shows where the variability in the molecules' fields can explain the observed target property differences. Figure 118 shows this representation for the three best CoMSIA models, while the same is shown for the other CoMSIA models in Figures 122-124.

Thus, as it can be observed in Figure 118 the main positive contribution to activity in model CoMSIA-4 comes from the presence of H-bond donor groups in the ligands close to the cyan region, which is next to the location of the NH of the protonated dimethylamino group of triazine **46**, shown in the figure. Negative contributions also arise from the presence of donor groups in regions close to the propyl chain and at both sides of the triazine ring, close to the NH groups bound to the phenethyl moieties in **46**.

Model CoMSIA-7 shows a similar distribution of cyan and purple regions but there is also an additional small cyan region close to the NH group that joints the propyl to the triazine moieties, suggesting that the presence of such NH donor group could improve the activity of the ligands. This is in agreement with the observation that replacing such NH by oxygen led to an important decrease of the activity (cf. triazine **46**, $pIC_{50}^{exp} = 7.30$, vs **50**, $pIC_{50}^{exp} = 5.21$). On the other hand CoMSIA-7 also shows a region (blue) that favors the presence of positive charges close to the protonated nitrogen and another minor one close to the para-substituent of one of the aromatic moieties. Finally, there are several red patches centered in the aromatic rings and regions close to the propyl chain that would disfavour the presence of positive charges, or favour the presence of electronegative groups, in those regions. Model CoMSIA-15 shows a similar distribution of favored and disfavored regions to CoMSIA-7, although the contributions of the aromatic rings are less important. Noteworthy, models CoMSIA-7 and -15, as well as other models that include both the donor and electrostatic fields (ie. CoMSIA-6 or -14, Table 15 and Figures 122-124), show that the variance is similarly partitioned among both field types (i.e. fraction donor ≈ fraction electrostatic). On the contrary, models that include the steric field (i.e. CoMSIA-5, -8, -13 and -16, Table 15 and Figures 122-124) show that this can only explain a small part (< 20 %) of the variance. This confirms that the changes in the activity of the training set can be

interpreted mainly in terms of the variation of their donor properties (CoMSIA-4) or their equally weighted donor plus electrostatic properties (CoMSIA-7 or -15). This was not surprising considering that most active compounds in the training set present a protonated cationic group that can also act as H-bond donor when interacting with the TRPV1 receptor. To better decide to what extent the determined biological activity depends on the donor and/or electrostatic properties of the ligands would require to have data for additional compounds that show a larger structural diversity.

Comparing the MIFs of each compound with the contours of the models is useful to interpret their predicted activities. Triazine **46**, the most active among the compounds synthesized, was correctly predicted as the most active compound by models CoMSIA-4 and CoMSIA-7. Its high predicted activity originates mainly from the good overlap between its donor MIF close to the protonated dimethylamino group (cyan contour in Figure 116, left) and the corresponding "favorable" region in model CoMSIA-4 (cyan contour in Figure 118, left). The other most intense donor MIF regions of **46** also overlap, although only partially, the "unfavorable" regions of CoMSIA-4 (purple contours in Figure 118, left), therefore their negative contribution is less important. A similar interpretation could be formulated for CoMSIA-7, although in this case the positive contributions to activity come not only from the intense donor MIF close to the protonated dimethylamino group, but also from the presence of the positive electrostatic field around it (blue contour in Figure 114, left) and the negative electrostatic field centered on the aromatic rings (red contours in Figure 114, left), which overlap well on the corresponding regions of model CoMSIA-7 (blue and red contours in Figure 118, center).

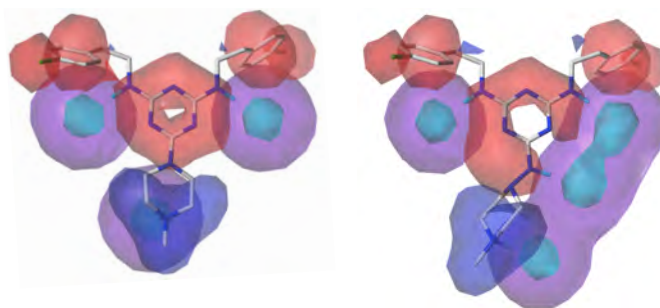**Figure 119.** CoMSIA donor (cyan and purple) and electrostatic (blue and red) MIFs of triazines **43** (left) and **45** (right), at 1.0 Å grid resolution and contoured at 80 (cyan and blue) and 20 % (purple and red).

Looking at the other end of the activity scale, triazine **43**, the less active one, shows a diferent distribution of its donor MIF relative to triazine **46**, particularly in the

location of the intense donor region close to the protonated tertiary nitrogen of the piperazine ring, which is closer to the triazine ring (Figure 119, left). This implies that this region is fully overlaped with one of the "unfavorable" donor contours that appear in model CoMSIA-4, and there is also a partial overlap of the other two intense donor MIF contours of **43**, those appearing close to the triazine-bound NH groups, with the other "unfavorable" regions of the same model. All of these negative contributions result in a very low predicted activity, which correlates well with the experimental observations. If the electrostatic MIF is also considered, the positive electrostatic field appears also shifted towards the triazine ring relative to its location in triazine **46**, therefore it does not overlap the positive "favourable" contour of model CoMSIA-7 (blue in Figure 118, center). On the contrary, it partially overlaps the two "unfavorable" regions at each side of the alkyl chain of triazine **46** (red in Figure 118, center), which contributes to a low predicted activity. Similar arguments could be elaborated if model CoMSIA-15 is taken in consideration. Thus, the three CoMSIA models agree in predicting triazine **43** as the less active of the full set of compounds considered.

In comparison with **43**, triazine **45** presents an additional NH group between the piperazine and triazine rings (Figure 119, right). This causes the protonated tertiary amine from the piperazine to be further appart from the triazine ring, such that the donor and positive electrostatic MIFs again overlap with the corresponding regions of models CoMSIA-4, -7 and -15. Therefore, this contributes positively to the predicted activity for this triazine despite its similarity to the less active **43**.

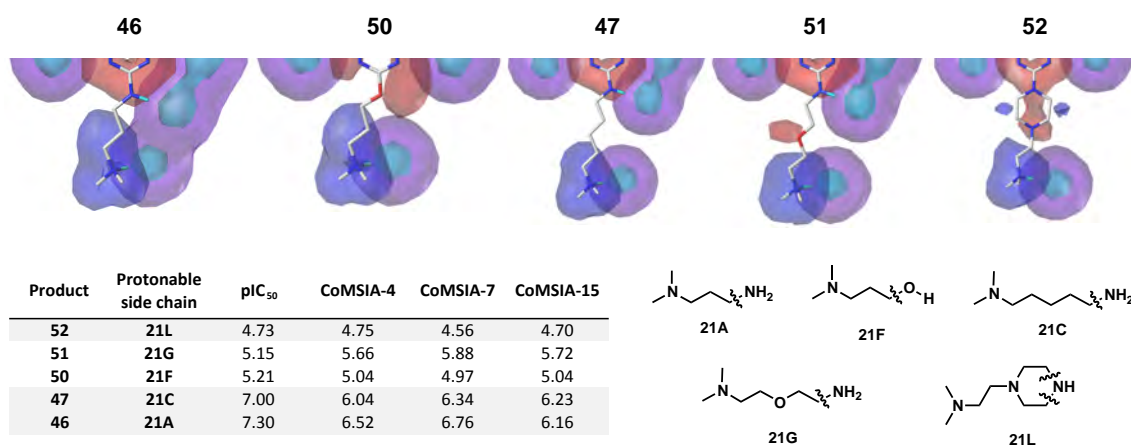| Product	Protonable side chain	pIC_{50}	CoMSIA-4	CoMSIA-7	CoMSIA-15
52	**21L**	4.73	4.75	4.56	4.70
51	**21G**	5.15	5.66	5.88	5.72
50	**21F**	5.21	5.04	4.97	5.04
47	**21C**	7.00	6.04	6.34	6.23
46	**21A**	7.30	6.52	6.76	6.16

Figure 120. CoMSIA donor (cyan and purple) and electrostatic (blue and red) MIFs of triazines **46**, **47**, **50**, **51** and **52**, at 1.0 Å grid resolution and contoured at 80 (cyan and blue) and 20 % (purple and red). The table shows their experimental and predicted pIC_{50} (M) values from models CoMSIA-4, -7 and -15.

Looking at the MIFs of other triazines that present different cationic side chains but share the rest of the structure, e.g. **46**, **47**, **50**, **51** and **52**, some differences are also apparent that could justify the different predicted activities (Figure 120). First, it looks that increasing the distance between the protonated dimethyl amine and the triazine (**46** vs **47**) is much less detrimental for activity than when it was decreased, as in **43**. This could be explained because the region occupied by the donor and positive electrostatic MIFs of the molecules can still overlap, at least partially, the favourable donor and positive electrostatic regions of models CoMSIA-4, -7 and -15. Triazines **50** and **51**, which also include an oxygen atom in their chains, show a furhter decrease in predicted activity. These correlates with a less intense donor field, apparent by the presence of a gap between the donor isocontours shown in Figure 120 for triazines **50** and **51**. This gap is even more important for triazine **52** due to the presence of the piperazine ring. From the electrostatic point of view, the differences between triazines **46** and **47** are minor, but the isocontours for the other three show more changes that also contribute to their decreased predicted activity. Altogether, the order of predicted activities for these 5 compounds correlates quite well with the experimental values from models CoMSIA-4 and CoMSIA-7, and slightly worse for CoMSIA-15.

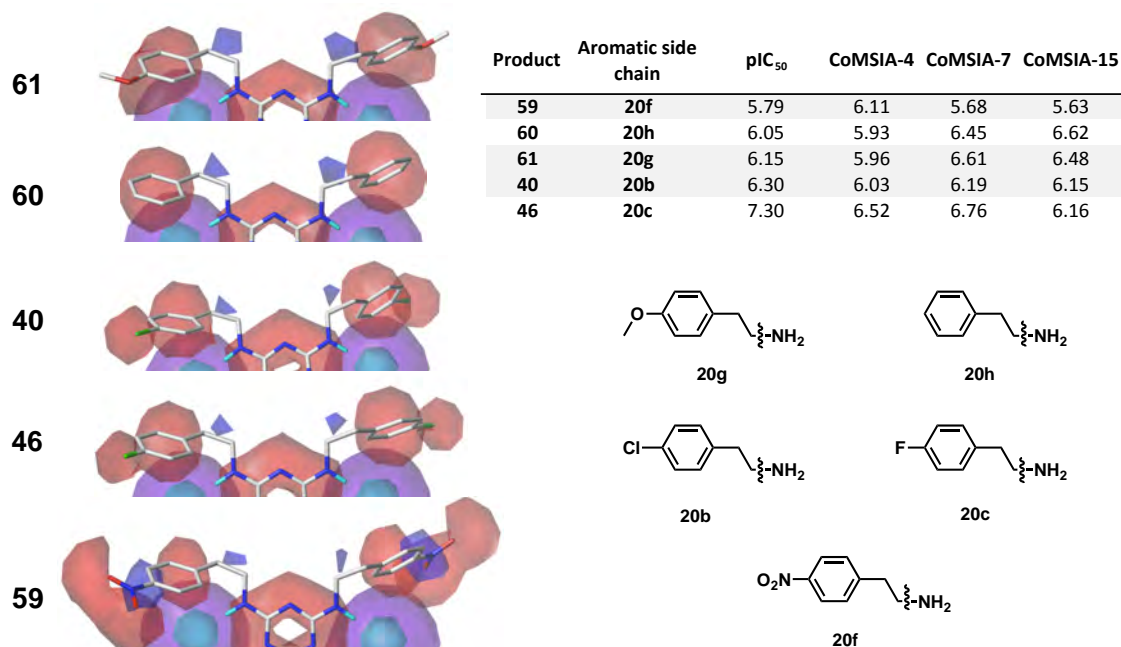| Product	Aromatic side chain	pIC_{50}	CoMSIA-4	CoMSIA-7	CoMSIA-15
59	20f	5.79	6.11	5.68	5.63
60	20h	6.05	5.93	6.45	6.62
61	20g	6.15	5.96	6.61	6.48
40	20b	6.30	6.03	6.19	6.15
46	20c	7.30	6.52	6.76	6.16

Figure 121. CoMSIA donor (cyan and purple) and electrostatic (blue and red) MIFs of triazines **40**, **46**, **59**, **60** and **61**, at 1.0 Å grid resolution and contoured at 80 (cyan and blue) and 20 % (purple and red). The table shows their experimental and predicted pIC_{50} (M) values from models CoMSIA-4, -7 and -15.

Similar comparisons could be carried out at the other side of the triazine system, where the two arylalkyl side chains are located. Figure 121 shows, for example, the donor and electrostatic MIFs of triazines **40**, **46**, **59**, **60** and **61**, whose structures only differ on the aromatic sustituent in para position and their activities cover a range of 1.5 log units (i.e. pIC_{50} = 5.8 - 7.3). The donor and electrostatic MIF representation show some variabilities in the electrostatic contours around the aromatic systems but no major changes in the donor contours, as expected since there are no hydrogen bonding groups involved in these moieties. The most active compounds of these group, **46** and **40**, present a similarly shaped negative electrostatic MIF contour centered in both the aromatic rings and the halogen atoms. In compounds **60** and **61** this contour is centered essentially on the aromatic ring, but in compound **59** is again separated in two regions, centered in the aromatic ring and the oxygens of the nitro groups, although a positive electrostatic contour appears between them. Both CoMSIA-4 and -7 can identify triazine **46** as the most active one among this group, but only CoMSIA-7 can identify triazine **59** as the less active one, and all the models are less succesful in finding the right activity order for the rest of the products in the group. This reflects the limited capacity of these models to accurately explain the activity variance that depends on this part of the molecules.

In summary, these results indicate that the two 3D-QSAR models derived from Alginment 1, CoMSIA-4 and -7, have a better predictive capacity than the one derived from Alignment 2, CoMSIA-15. The results also suggest that the TRPV1 antagonist activity of the collection of compounds considered depends mainly on their properties as hydrogen-bond donors and also, despite the slightly worse statistics of model CoMSIA-7 relative to CoMSIA-4, on their electrostatic properties. In these sense, explaining the variance in terms of two types of contribution (donor and electrostatic) makes easier to rationalize and visualize which structural changes might explain the activities observed and to make hypothese about which structural modifications can be introduced to improve the activity of the compounds. As general trends of activity, the models suggested that:

- there is a distance constraint for the location of the donor/cationic group relative to the triazine ring, being 5-6 bonds from the triazine ring the right distance,

- the presence of donor groups at the attachment position between the aryl-supporting side chain and the triazine ring can be detrimental,

- the presence of donor groups at the cation-supporting chain attachment position can be slightly beneficial, but the presence of electronegative groups like oxygen is deleterious,

- although the activity seems less dependent on the substitution on the two aryl moieties, it appears that an intense negative electrostatic field centered between the aromatic group and its substituents in para position, without any positive electrostatic field, is good for the activity.

- the models support the binding hypothesis shown in Figure 108, at the beginning of this chapter, that postulates that the most active ones could interact at the entrance of the TRPV1 channel by inserting their cationic-alkyl group in the pore, and that in this interaction, hydrogen bonding and electrostatic ineractions play a central role.

Despite the limitations due to the reduced number of compounds taken in consideration and their relatively small chemical diversity, the 3D-QSAR models generated constituted a first approach to predict the activities of new compounds. As it is shown in the next chapter, they were succesfully applied in the prediction of the activity of a few newly designed compounds, supporting their aplicability as predictive tools for structurally related molecules.

Table 15. [a] Leave-one-out q^2. [b] Leave-one-out PRESS. [c] Number of components. [d] Average q^2 from 10 runs of random groups cross validation (10 groups). [e] Average PRESS from 10 runs of random groups cross validation (10 groups). [f] Standard error of estimate. [g] Standard deviation of residuals.

Training set	CoMFA-1	CoMFA-2	CoMSIA-1	CoMSIA-2	CoMSIA-9	CoMSIA-10
Alignment	1	2	1	1	2	2
q^2 (LOO)[a]	0.22	0.21	0.29	0.46	0.27	0.42
PRESS (LOO)[b]	1.65	1.67	1.62	1.51	1.67	1.5
N[c]	1	1	3	5	3	3
Fraction:						
Steric				1		1
Electrostatic				1		1

Training set	CoMSIA-3	CoMSIA-4	CoMSIA-5	CoMSIA-6	CoMSIA-7	CoMSIA-8	CoMSIA-11	CoMSIA-12	CoMSIA-13	CoMSIA-14	CoMSIA-15	CoMSIA-16
Alignment	1	1	1	1	1	1	2	2	2	2	2	2
q^2 (LOO)[a]	0.54	0.66	0.62	0.57	0.60	0.57	0.53	0.58	0.49	0.54	0.56	0.56
PRESS (LOO)[b]	1.33	1.17	1.24	1.28	1.27	1.31	1.34	1.30	1.44	1.33	1.33	1.34
N[c]	3	4	4	3	4	4	3	4	4	3	4	4
q^2 (CV)[d]	0.58 ± 0.03	0.65 ± 0.03	0.56 ± 0.03	0.58 ± 0.03	0.58 ± 0.03	0.58 ± 0.03	0.49 ± 0.02	0.54 ± 0.04	0.43 ± 0.06	0.53 ± 0.02	0.57 ± 0.03	0.52 ± 0.04
PRESS (CV)[e]	1.27 ± 0.05	1.19 ± 0.05	1.19 ± 0.05	1.30 ± 0.05	1.27 ± 0.03	1.32 ± 0.02	1.40 ± 0.03	1.37 ± 0.05	1.51 ± 0.08	1.34 ± 0.02	1.32 ± 0.04	1.39 ± 0.05
SEE[f]	0.73	0.70	0.64	0.51	0.41	0.40	0.81	0.81	0.66	0.52	0.44	0.42
r^2	0.86	0.88	0.90	0.93	0.96	0.96	0.83	0.84	0.81	0.93	0.95	0.96
F-value	43.10	35.80	43.70	97.50	115.90	121.80	34.50	25.80	41.10	94.00	100.40	111.60
Fraction:												
Steric			0.19			0.10			0.18			0.08
Electrostatic				0.50	0.49	0.44				0.54	0.55	0.50
Donor	1.00	1.00	0.81	0.50	0.51	0.46	1.00	1.00	0.82	0.46	0.45	0.42
Test set												
r^2	0.80	0.88	0.85	0.84	0.79	0.80	0.81	0.87	0.87	0.79	0.73	0.77
SD res.[g]	0.49	0.41	0.38	0.58	0.55	0.59	0.44	0.41	0.37	0.69	0.70	0.70

Figure 122. CoMSIA models built from Alignment 1. First row shows isocontours of field contribution (StDev*Coeff) overlaid on molecule **46** for each model. CoMSIA models are represented by positive (or "favoured", 80 %) and negative (or "unfavoured", 20 %) interaction surfaces: green and yellow for steric field, blue and red for the electrostatic one and cyan and purple for the donor field. Lower rows represent the experimental vs predicted activity, pIC$_{50}$ (M), and the residuals for all compounds. Products are represented as: Training set (◊), Test set (▲) and Outliers (★).
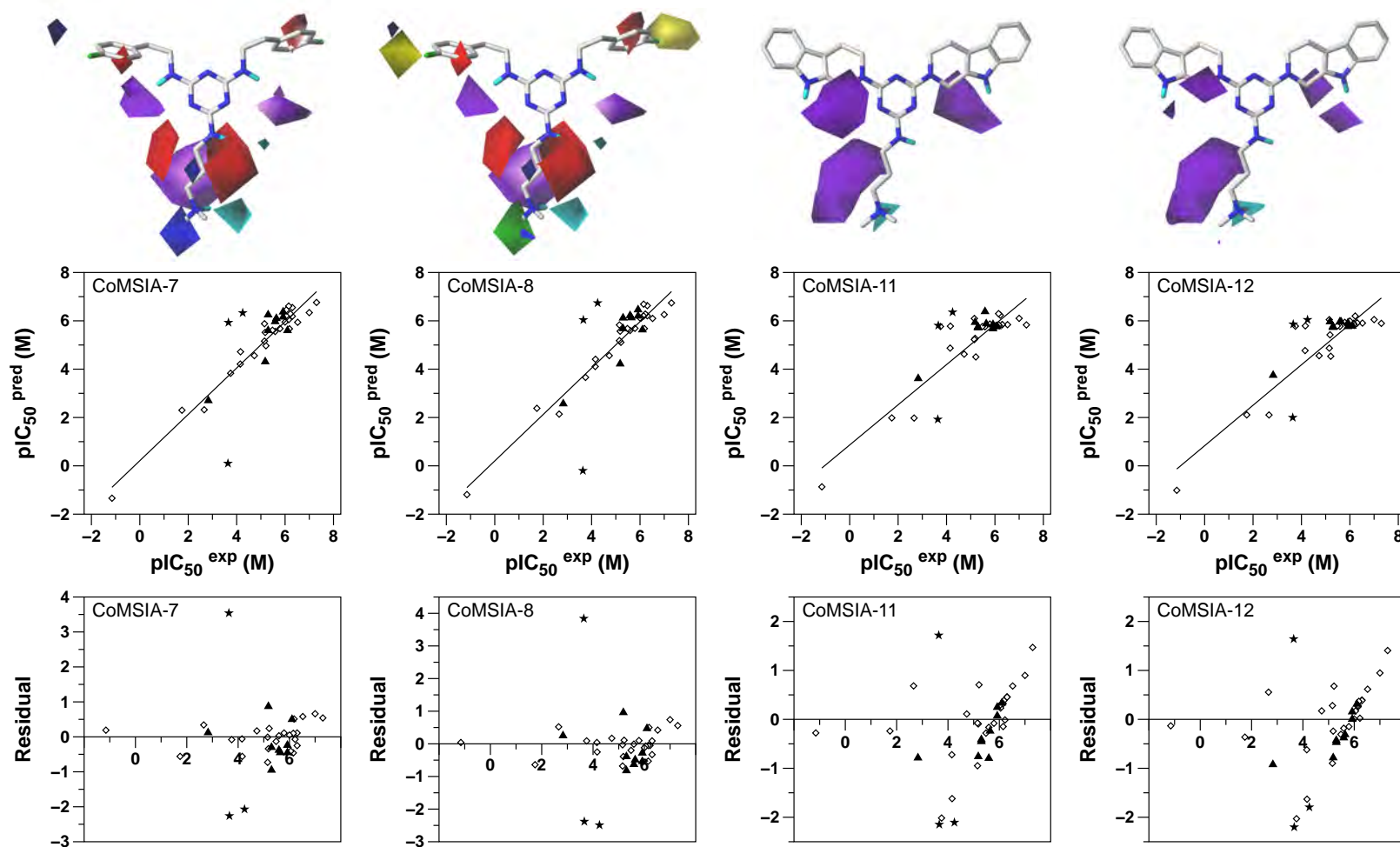
Figure 123. CoMSIA models built from alignment 1 (CoMSIA-7 and -8) and 2 (CoMSIA-11 and -12). First row shows contours of field contribution (StDev*Coeff) overlaid on molecules **46** (COMSIA-7 and -8) and **72** (CoMSIA-11 and -12) for each model. CoMSIA models are represented by positive (or "favoured", 80 %) and negative (or "unfavoured", 20 %) interaction surfaces: green and yellow for steric field, blue and red for the electrostatic one and cyan and purple for the donor field. Lower rows represent the experimental vs predicted activity, pIC_{50} (M), and the residuals for all compounds. Products are represented as: Training set (◊), Test set (▲) and Outliers (★).
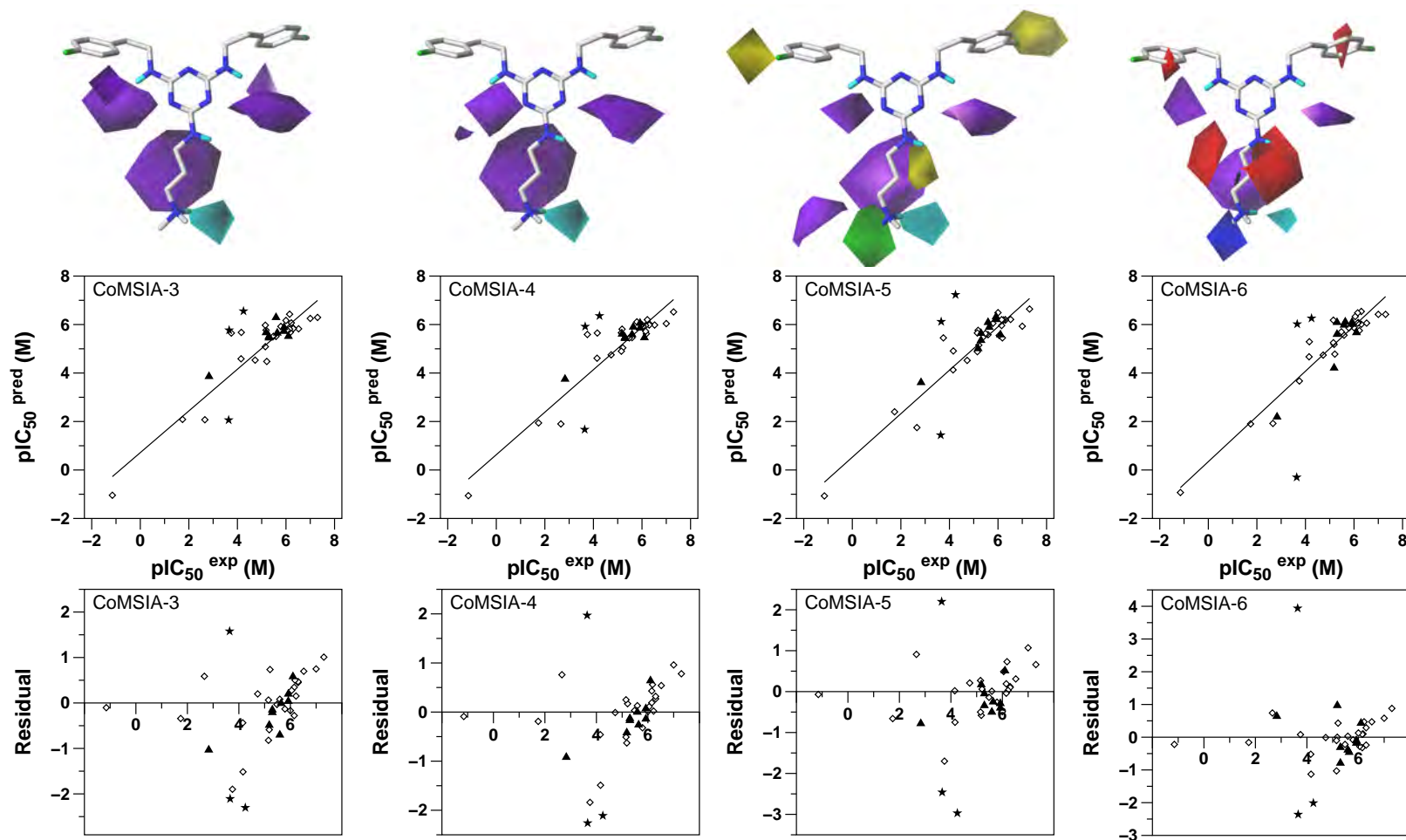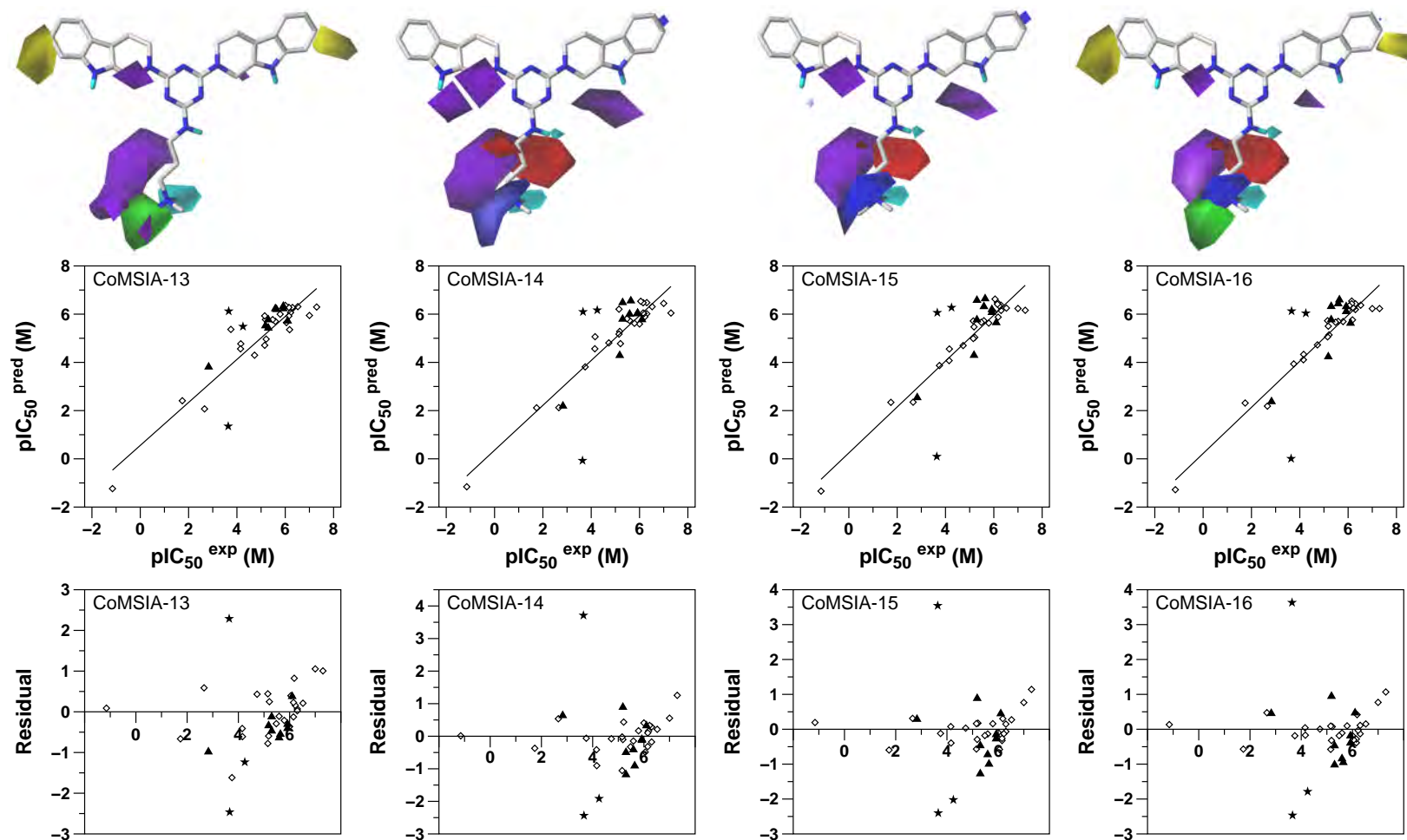
Figure 124. CoMSIA models built from alignment 2. First row shows contours of field contribution (StDev*Coeff) overlaid on molecule **72** for each model. CoMSIA models are represented by positive (or "favoured", 80 %) and negative (or "unfavoured", 20 %) interaction surfaces: green and yellow for steric field, blue and red for the electrostatic one and cyan and purple for the hydrogen bond donor field. Lower rows represent the experimental vs predicted activity, pIC_{50} (M), and the residuals for all compounds. Products are represented as: Training set (◊), Test set (▲) and Outliers (★).

**Table 16.** Experimental and predicted pIC$_{50}$ (M) values and residuals, determined from CoMSIA-3 to CoMSIA-8 models.

Compound	pIC$_{50}$^{exp}	CoMSIA-3 pIC$_{50}$^{pred}	Res.	CoMSIA-4 pIC$_{50}$^{pred}	Res.	CoMSIA-5 pIC$_{50}$^{pred}	Res.	CoMSIA-6 pIC$_{50}$^{pred}	Res.	CoMSIA-7 pIC$_{50}$^{pred}	Res.	CoMSIA-8 pIC$_{50}$^{pred}	Res.
46	7.30	6.29	1.01	6.52	0.78	6.64	0.66	6.42	0.88	6.76	0.54	6.74	0.56
47	7.00	6.25	0.75	6.04	0.96	5.93	1.07	6.42	0.58	6.34	0.66	6.26	0.74
57	6.52	5.83	0.70	5.98	0.54	6.21	0.31	6.06	0.47	5.94	0.58	6.10	0.42
40	6.30	5.85	0.45	6.03	0.27	6.18	0.12	6.01	0.29	6.19	0.11	6.21	0.09
58	6.30	5.83	0.47	5.98	0.32	6.20	0.10	6.54	-0.24	6.55	-0.25	6.63	-0.33
48	6.22	6.07	0.15	6.20	0.02	6.19	0.03	5.75	0.47	6.29	-0.07	6.28	-0.05
66	6.18	5.68	0.50	5.62	0.56	5.45	0.73	6.08	0.10	5.67	0.51	5.68	0.50
61	6.15	5.81	0.34	5.96	0.19	6.20	-0.04	6.48	-0.32	6.61	-0.46	6.69	-0.53
DD-161515	6.15	6.43	-0.28	5.72	0.43	5.96	0.19	6.06	0.09	6.05	0.10	6.20	-0.05
60	6.05	5.77	0.28	5.93	0.11	5.55	0.49	6.33	-0.28	6.45	-0.41	6.12	-0.07
44	6.00	6.17	-0.17	5.99	0.01	6.49	-0.49	5.87	0.13	5.95	0.05	6.12	-0.12
59	5.79	5.92	-0.13	6.11	-0.32	6.05	-0.26	5.86	-0.08	5.68	0.11	5.69	0.10
62	5.59	5.51	0.08	5.46	0.13	5.58	0.01	5.56	0.03	5.56	0.03	5.60	-0.01
65	5.48	5.51	-0.03	5.45	0.03	5.63	-0.14	5.70	-0.22	5.61	-0.13	5.68	-0.20
50	5.21	4.48	0.74	5.04	0.17	5.15	0.06	4.78	0.43	4.97	0.24	5.11	0.11
45	5.18	5.77	-0.59	5.81	-0.63	5.76	-0.58	5.18	0.00	5.52	-0.34	5.57	-0.39
51	5.15	5.97	-0.82	5.66	-0.51	5.65	-0.50	6.18	-1.03	5.88	-0.73	5.83	-0.68
72	5.15	5.09	0.06	4.90	0.25	4.88	0.27	5.25	-0.10	5.16	-0.01	5.18	-0.03
52	4.73	4.53	0.20	4.75	-0.01	4.52	0.21	4.74	-0.01	4.56	0.17	4.56	0.17
68	4.16	5.68	-1.52	5.65	-1.49	4.91	-0.75	5.29	-1.13	4.72	-0.56	4.41	-0.25
53	4.15	4.59	-0.44	4.61	-0.46	4.13	0.02	4.67	-0.52	4.21	-0.06	4.11	0.04
69	3.75	5.65	-1.90	5.59	-1.84	5.45	-1.70	3.67	0.08	3.83	-0.08	3.66	0.09
55	2.66	2.07	0.59	1.90	0.76	1.75	0.91	1.92	0.74	2.32	0.34	2.14	0.52
56	1.74	2.09	-0.34	1.94	-0.19	2.40	-0.66	1.90	-0.16	2.30	-0.56	2.38	-0.64
43	-1.15	-1.04	-0.10	-1.06	-0.09	-1.07	-0.07	-0.93	-0.22	-1.34	0.19	-1.19	0.04
64	6.10	5.52	0.58	5.46	0.64	5.58	0.51	5.67	0.43	5.60	0.50	5.63	0.47
42	5.92	5.72	0.20	5.86	0.07	6.32	-0.40	6.02	-0.10	6.37	-0.45	6.46	-0.54
17	5.92	5.88	0.04	6.06	-0.14	6.21	-0.29	6.10	-0.18	6.16	-0.24	6.20	-0.28
71	5.64	5.65	-0.01	5.90	-0.26	5.89	-0.25	6.11	-0.46	6.10	-0.45	6.13	-0.49
DD-191515	5.59	6.29	-0.70	5.59	0.00	6.09	-0.50	5.98	-0.39	5.97	-0.38	6.22	-0.63
67	5.30	5.45	-0.15	5.43	-0.13	5.35	-0.05	6.09	-0.79	6.25	-0.95	6.12	-0.82
63	5.30	5.51	-0.21	5.47	-0.17	5.64	-0.34	5.60	-0.31	5.60	-0.30	5.68	-0.39
41	5.18	5.67	-0.49	5.61	-0.42	5.01	0.17	4.21	0.97	4.31	0.87	4.22	0.96
54	2.83	3.86	-1.03	3.75	-0.92	3.61	-0.78	2.19	0.64	2.70	0.12	2.57	0.25
73	4.25	6.56	-2.30	6.36	-2.11	7.23	-2.97	6.26	-2.01	6.33	-2.07	6.74	-2.49
74	3.66	5.77	-2.11	5.92	-2.26	6.12	-2.46	6.02	-2.36	5.93	-2.26	6.04	-2.38
70	3.64	2.06	1.58	1.67	1.97	1.44	2.20	-0.30	3.94	0.0	3.54	-0.20	3.84

Table 17. Experimental and predicted pIC$_{50}$ (M) values and residuals, determined from CoMSIA-11 to CoMSIA-16 models.

Compound	pIC$_{50}$^{exp}	CoMSIA-11		CoMSIA-12		CoMSIA-13		CoMSIA-14		CoMSIA-15		CoMSIA-16	
		pIC$_{50}$^{pred}	Res.	pIC$_{50}$^{pred}	Res.	pIC$_{50}$^{pred}	Res.	pIC$_{50}$^{pred}	Res.	pIC$_{50}$^{pred}	Res.	pIC$_{50}$^{pred}	Res.
46	7.30	5.83	1.47	5.90	1.41	6.30	1.01	6.05	1.26	6.16	1.14	6.23	1.07
47	7.00	6.10	0.90	6.05	0.95	5.95	1.05	6.45	0.55	6.23	0.77	6.23	0.77
57	6.52	5.84	0.68	5.91	0.62	6.31	0.21	6.31	0.21	6.25	0.27	6.37	0.15
40	6.30	5.84	0.46	5.91	0.39	6.23	0.07	6.02	0.29	6.15	0.15	6.19	0.11
58	6.30	5.85	0.45	5.92	0.39	6.28	0.03	6.48	-0.18	6.37	-0.07	6.43	-0.13
48	6.22	6.23	-0.01	6.20	0.02	6.06	0.16	5.89	0.33	6.35	-0.13	6.26	-0.03
66	6.18	5.80	0.38	5.81	0.37	5.36	0.82	6.02	0.16	5.88	0.30	5.76	0.42
61	6.15	5.83	0.32	5.90	0.26	6.28	-0.13	6.47	-0.32	6.48	-0.32	6.54	-0.39
DD-161515	6.15	6.30	-0.15	5.86	0.29	5.92	0.23	6.05	0.10	6.41	-0.26	6.43	-0.28
60	6.05	5.81	0.23	5.87	0.17	5.65	0.40	6.53	-0.49	6.62	-0.58	6.35	-0.30
44	6.00	5.72	0.28	5.99	0.01	6.36	-0.36	5.59	0.41	6.09	-0.09	6.19	-0.18
59	5.79	5.87	-0.08	5.94	-0.15	6.00	-0.21	5.62	0.17	5.63	0.16	5.69	0.10
62	5.59	5.75	-0.16	5.77	-0.18	5.70	-0.11	5.74	-0.15	5.73	-0.14	5.70	-0.11
65	5.48	5.76	-0.28	5.79	-0.31	5.77	-0.29	5.81	-0.33	5.66	-0.18	5.67	-0.18
50	5.21	4.51	0.71	4.53	0.68	4.96	0.25	4.78	0.43	5.04	0.17	5.14	0.07
45	5.18	5.27	-0.09	5.42	-0.24	5.78	-0.59	5.28	-0.10	5.47	-0.29	5.50	-0.32
51	5.15	6.10	-0.95	6.05	-0.90	5.93	-0.78	6.21	-1.05	5.72	-0.57	5.73	-0.58
72	5.15	5.23	-0.08	4.87	0.28	4.71	0.44	5.17	-0.02	4.99	0.16	5.06	0.09
52	4.73	4.62	0.11	4.56	0.17	4.30	0.43	4.81	-0.08	4.70	0.03	4.73	0.01
68	4.16	5.78	-1.62	5.79	-1.63	4.77	-0.61	5.06	-0.90	4.56	-0.39	4.33	-0.17
53	4.15	4.87	-0.72	4.77	-0.62	4.56	-0.41	4.56	-0.41	4.07	0.08	4.11	0.04
69	3.75	5.77	-2.02	5.78	-2.03	5.37	-1.62	3.81	-0.06	3.87	-0.12	3.94	-0.19
55	2.66	1.98	0.68	2.11	0.56	2.07	0.59	2.12	0.54	2.35	0.31	2.19	0.47
56	1.74	1.98	-0.24	2.11	-0.36	2.41	-0.66	2.12	-0.37	2.34	-0.60	2.31	-0.57
43	-1.15	-0.87	-0.28	-1.01	-0.13	-1.24	0.09	-1.16	0.01	-1.34	0.19	-1.28	0.13
64	6.10	5.76	0.33	5.79	0.31	5.72	0.38	5.77	0.32	5.65	0.45	5.63	0.47
42	5.92	5.67	0.25	5.77	0.16	6.33	-0.41	6.02	-0.10	6.19	-0.27	6.31	-0.39
17	5.92	5.85	0.07	5.92	0.00	6.23	-0.31	6.05	-0.12	6.07	-0.15	6.11	-0.19
71	5.64	5.88	-0.24	5.95	-0.31	6.19	-0.55	6.55	-0.91	6.64	-1.00	6.60	-0.95
DD-191515	5.59	6.39	-0.79	5.97	-0.38	6.23	-0.64	6.00	-0.41	6.32	-0.73	6.43	-0.84
67	5.30	5.71	-0.41	5.73	-0.43	5.42	-0.12	6.48	-1.18	6.58	-1.28	6.32	-1.02
63	5.30	5.75	-0.45	5.77	-0.47	5.77	-0.47	5.79	-0.50	5.77	-0.47	5.77	-0.47
41	5.18	5.94	-0.76	5.96	-0.78	5.52	-0.34	4.29	0.89	4.30	0.89	4.24	0.95
54	2.83	3.61	-0.79	3.75	-0.92	3.81	-0.98	2.19	0.64	2.54	0.29	2.37	0.45
73	4.25	6.36	-2.11	6.05	-1.79	5.49	-1.24	6.17	-1.92	6.27	-2.02	6.04	-1.79
74	3.66	5.81	-2.15	5.86	-2.20	6.12	-2.46	6.10	-2.44	6.06	-2.40	6.13	-2.47
70	1.92	1.72	2.00	1.64	1.35	2.29	-0.07	3.71	0.10	3.54	0.01	3.63	1.92